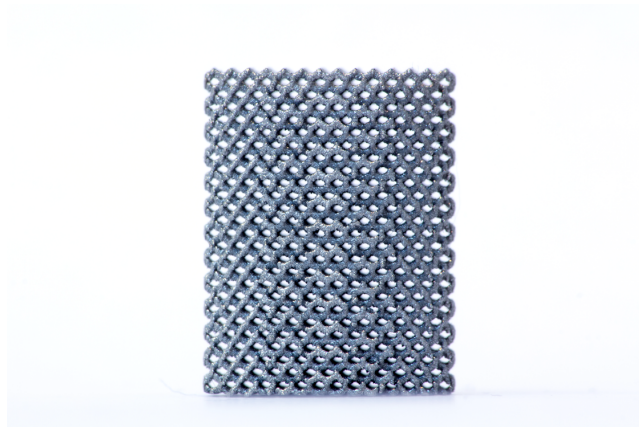


The effect of stress ratio on the fatigue behavior of additively manufactured porous biomaterials

by

Joep de Krijger

to obtain the degree of Master of Science
at the Delft University of Technology,
to be defended on March 8 , 2016 at 1:00 PM.



Student number: 4248260
Project duration: Februari 1, 2015 – March 8, 2016
Thesis committee: Dr. A. A. Zadpoor TU Delft, supervisor, Chairman
Dr. C. D. Rans TU Delft, supervisor
Prof. Dr. J. Sietsma TU Delft
Dr. B. Van Hooreweder KU Leuven

This thesis is confidential and cannot be made public until March 8, 2017.

An electronic version of this thesis is available at
<http://repository.tudelft.nl/>.

[This page intentionally left blank]

Acknowledgments

I would like to thank my supervisors Calvin Rans and Amir Zadpoor for their guidance and help during this Thesis. Their enthusiasm about research in additive manufacturing made me choose to perform my thesis study in this field. The tips and feedback that I got during the whole project were very useful and helped me becoming a better researcher. Also their confidence in the possibility to publish my research gave me extra motivation during this project.

I would like to thank Gertjan Mulder from the Aerospace lab for supporting me with the image correlation and fatigue tests, and always taking time to explain and help me if I ran into a problem. Also I would like to thank Sander Leeftang from the BME department for helping me with the compression tests, and Behdad Pouran for the micro-CT scans during an educational morning in Utrecht. Also his help with processing the results in ImageJ was greatly appreciated.

Then I would like to thank the members from the 'koffiecorner' for the nice working environment and sometimes much needed coffee breaks. I appreciated the ability to discuss my work with other students that were not working on the same subject, making it possible to look at my project from different perspectives.

Finally I would like to thank my parents for their support during my masters, the rest of the family for their interest in my project and especially my girlfriend Lisan for her patience and encouragement during my thesis.

Nomenclature

Abbreviations

AD	Apparent Density
CAD	Computer Aided Design
DIC	Digital Image Correlation
EBM	Electron Beam Melting
EDM	Electrical Discharge Machining
EP	Electro Polished
HIP	Hot Isostatic Pressing
SLM	Selective Laser Melting
SN	Stress versus N cycles
SP	Shot Peening
SR	Stress Relieve
STL	Surface Tessellation Language
VAR	Vacuum Arc Remelted

Symbols

E	Energy Density	$[Jm^{-3}]$
P	Laser Power	$[Js^{-1}]$
v	Scanning Speed	$[ms^{-1}]$
h	Hatch Spacing	$[m]$
t	Layer Thickness	$[m]$
K	Stress Intensity Factor	$[MPa\sqrt{m}]$
σ	Stress	$[MPa]$
a	Crack Length	$[m]$
W	specimen Width	$[m]$
R	Stress Ratio	$[-]$
S_a	Stress Amplitude	$[MPa]$
σ_a	Stress Amplitude	$[MPa]$
σ_m	Mean Stress	$[MPa]$
σ_y	Yield Stress	$[MPa]$
σ_u	Ultimate Stress	$[MPa]$
σ_{-1}	Reversed Stress amplitude (At $R = -1$)	$[MPa]$
σ_{max}	Maximum Stress	$[MPa]$
σ_{off}	Offset Stress (Yield Stress)	$[MPa]$
σ_{pl}	Plateau Stress	$[MPa]$
e_{max}	Strain at maximum stress	$[\%]$
$E.A.$	Energy Absorption	$[MJm^{-3}]$
E_{20-70}	Quasi Elastic Gradient	$[GPa]$

Contents

1	Introduction	1
2	Background	3
2.1	Biomaterials	3
2.2	Selective Laser Melting	5
2.3	Meta-materials	6
2.4	Fatigue theory	7
2.4.1	Crack Initiation	7
2.4.2	Crack growth	8
2.4.3	Scatter	9
2.4.4	SN curves and Fatigue diagrams	9
2.5	Fatigue behavior of Ti-6Al-4V and slm Ti-6Al-4V	13
2.5.1	Ti-6Al-4V	13
2.5.2	Fatigue behavior of Ti-6Al-4V	15
2.5.3	Fatigue behavior of Ti-6Al-4V produced by selective laser melting	20
2.5.4	Meta-biomaterial	25
3	Materials and Methods	26
3.1	Materials and manufacturing	26
3.2	Morphological characterization	27
3.3	Static mechanical testing	27
3.4	Fatigue Testing	28
3.5	Digital Image Correlation	29
4	Results	30
4.1	Characterization	30
4.2	Mechanical testing	30
4.3	Fatigue testing	31
4.4	Digital image correlation	34
5	Discussion	37
6	Conclusions and Recommendations	43
6.1	Conclusions	43
6.2	Recommendations	44
A	Matlab code DIC	51

B	Extra Images DIC	53
C	Compression Test and DIC	54
D	Sample overview	57
E	Paper abstract and introduction	60

Chapter 1

Introduction

The fatigue behavior of meta-biomaterials produced by Selective Laser Melting is investigated during this project. Meta-biomaterials are meta-materials for biomedical applications such as bone implants or prosthetics. Meta-materials are materials that derive their macroscopic properties from their micro-architecture, which is in case of meta-biomaterials a repeating unit cell that is made of small struts. Problems associated with this area of study can be divided into three parts. The first part is the biological behavior of these materials, which mainly focuses on osseointegration. This refers to the interaction between an implant and human tissue which includes bone ingrowth and cell attachment to the material. The second part are the mechanical properties. Studies in this area are for example aimed at the effect of variations in unit cell designs, porosity values and microstructures on different properties such as yield strength, modulus of elasticity and fatigue strength. A third subject associated with this research area is the Selective Laser Melting process. Selective Laser Melting (SLM) is an additive manufacturing process, that uses a high power laser to subsequently melt layers of metal powder to form a product. The effect of the process parameters and for example build orientations have been under investigation in previous studies.

This research is focused on the fatigue behavior of porous biomaterials (meta-biomaterials). Fatigue is failure of a material due to cyclic loading that results in the development of cracks in the material. The effect of mean stress (or stress ratio, R) on a diamond unit cell structure is investigated. There are several other studies about the fatigue behavior of these type of materials, which for example is aimed at the effects of different unit cells and porosity values. The fatigue tests have all been performed at a stress ratio of 0.1, meaning that the maximum stress in a fatigue cycle is ten times the minimum stress. Often the material properties of meta-materials are compared to the bulk material. This can also be done for meta-biomaterials made of Ti-6Al-4V. It is known that the fatigue strength of this material decreases with increasing mean stress that occurs at higher stress ratios. This raises the question if this decrease of the fatigue strength also occurs in meta-biomaterials that are built up of unit cells instead of a solid material.

Knowledge about the fatigue behavior of meta-biomaterials is important because of its application in for example bone implants. Bone implants usually require to withstand a year of cyclic loading, which can be translated into almost

1 million cycles based on one hour movement at 1Hz every day. It is also important for general understanding of this type of materials, and it can provide new insights for further research.

The objective of this research is to gain more knowledge on the R-ratio behavior of porous biomaterials. Therefore practical fatigue tests are carried out at stress ratios of $R=0.1$, $R=0.3$, $R=0.5$, $R=0.7$ and $R=0.8$. For each stress ratio, an SN curve is constructed. The SN curves can then be combined to create a constant life diagram. A constant life diagram or fatigue diagram is used to describe the mean stress behavior, by plotting the mean stress against the stress amplitude for different fatigue lives. This makes it possible to compare the test results with literature. Fatigue tests are very time consuming, but can yield to interesting results and based on the results of this study, more specific and better decisions could be made for further research on this topic. Next to the fatigue tests, an experimental Digital Image Correlation (DIC) method is developed to visualize the gradual failure to aid in understanding the observed behavior.

This thesis consists of six chapters, from which chapter three to six have been combined into a scientific paper. The abstract and introduction of this paper are removed from the report because it does not provide any new information. For completeness, the abstract and introduction are added in appendix E. The introducing chapter one is followed by a summary of the related literature in chapter two, starting with a general description of biomaterials and fatigue theory. The second part of this chapter consists of a description of previous work on the fatigue behavior of Ti-6Al-4V, SLM produced Ti-6Al-4V and porous materials produced with SLM. The third chapter consists of a description of the used materials, methods and procedures after which the results are presented in chapter four. Chapter five provides a discussion of the results, followed by a list of conclusions in chapter six. This chapter also includes recommendations for further research. The appendix contains the Matlab code that is used for the Digital Image Correlation measurements, together with some extra images that were processed with this method. Also a list of all fatigue tests that were performed during this research is provided in the appendix.

Chapter 2

Background

2.1 Biomaterials

The definition of a biomaterial has changed over time due to technological development and the increasing number of functions and requirements that are applied to a biomaterial. One of the first structured definitions[1](1987) that could nowadays still be used, is as follows:

A biomaterial is a non-viable material used in a medical device, intended to interact with biological systems

Biomaterials refer to materials that are used in a variety of applications such as joint replacements, bone fixations, blood vessel prosthesis, heart valves, skin substitutes, but also contact lenses. Each application has different requirements resulting in a variety of material classes that are used.

The most important requirement for all biomaterials is biocompatibility. This concept has also many definitions, which developed from just the ability of a material to be in contact with a living system without producing an adverse effect, into a more actively supporting role. This for example includes the ability to promote the formation of new tissue [2].

A summary of different biomaterials and material classes with some examples of applications are summarized in table 2.1.

Table 2.1: Biomaterials with some typical applications[2]

Material class	Typical applications
Metals	Load-bearing orthopaedic implants, Dental implants, endovascular stents
Ceramics	Orthopaedic and dental implants, Bone cements, heart-valve components
Polymers	vascular prosthesis, skin/cartilage, coatings and fillers, suture
Natural/tissue-derived materials	Tissue reconstruction and repair, arteries, veins
composites	Cardiovascular catheters, textile vascular prostheses

As can be seen from this table, metals have their main application in the

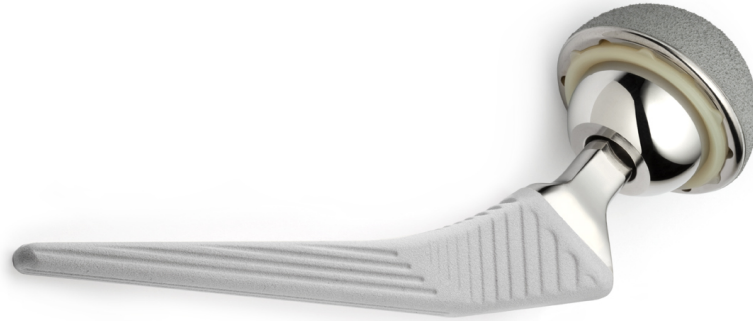


Figure 2.1: Metal Hip implant [4]

orthopaedic implants. These type of implants require the ability to withstand cyclic loads and require high strength, ductility, and corrosion resistance. In order to fixate the implant with the bone, the implant needs to integrate with the bone structure which is a process called osseointegration. Osseointegration requires a porous surface onto which bone tissue can grow. An example of a conventional implant with such a surface is displayed in Figure 2.1. The three most common metals used in orthopedics are stainless steel alloys, titanium alloys and cobalt alloys. An overview of the mechanical properties of bone and some biometals are presented in Table 2.2. Titanium is the most commonly used metal, because of its low density, high corrosion resistance and lower modulus compared to stainless steel and cobalt chrome. A downside of titanium is its low hardness, which could lead to abrasive wear. Cobalt alloys have both a high wear resistance and fatigue strength. Stainless steels have the lowest cost and are relatively easy to process, which makes them most suitable for temporary devices such as fracture plates and screws[3].



Figure 2.2: Integrated bone scaffolds [5]

A new group of biometals that are now developed by using new production techniques such as Selective Laser Melting (SLM) are metallic macroporous structures. These materials are built-up from repeating unit cells which makes it possible to adapt the mechanical properties by varying the unit cell type and strut thickness. An example of such a porous structure implemented in a bone implant can be seen in Figure 2.2. The relative low stiffness of these structures prevent stress shielding and the open cells allow for bone ingrowth.

Stress shielding occurs when a harder or stronger (implant) material absorbs the stresses that are transmitted through the body because of its higher stiffness. The bone tissue adapts to the lower load conditions by disintegrating, which is unfavourable.

Another advantage of the selective laser melting process is the ability to produce patient specific parts. A more detailed explanation of the Selective Laser Melting process and its advantages and disadvantages are given in section 2.2.

Table 2.2: Mechanical properties of common Bio-metals [6]

Material	E (GPa)	YS (MPa)	UTS (MPa)
Bone	15-30	30-70	70-150
Ti-6Al-4V	110	850-900	960-970
316 S.S.	210	240	600
CoCr	225	525	735

2.2 Selective Laser Melting

Selective Laser Melting is an additive manufacturing production process. Additive manufacturing processes are based on building up a part by subsequent layers opposed to conventional subtracting manufacturing techniques such as CNC milling. The additive manufacturing production technique has two major advantages over the conventional techniques. The first advantage is that this method makes it possible to create parts that are impossible to create with conventional techniques. For example a part with internal cavities and complex geometries. The second advantage of additive manufacturing is that it is very cost effective for low batch sizes. Each part can be made individually without the need of expensive moulds and tools. The machine only needs a 3d CAD file. This is especially useful in the biomedical industry, because this makes it possible to create patient specific parts.

The selective laser melting process starts by loading the designed CAD file into the machine. This is usually in the form of an STL file, which is a binary file that uses triangular facets to approximate the part. The software then creates different cross sections, that are radiated by a laser beam. Figure 2.3 shows a schematic of a selective laser melting machine. The parts are built on a solid substrate, by applying a layer of powder on top and radiating it with a laser to locally melt the powder which then solidifies. The build platform then lowers and a new layer of powder is put on top. This process repeats until the part is fully built, after which the powder is removed. The part is then detached from the build platform by wire Electrical Discharge Machining (EDM) or other techniques. The printer parameters can be characterised with an energy density $E(Jm^{-3})$ that is applied during scanning of a layer, which is defined by formula 2.1 [8]. In this formula, P is the laser power in Js^{-1} , v is the scanning speed(ms^{-1}), h is the hatch spacing(m), which is the distance between two consecutive scan vectors, and t is the layer thickness in m .

$$E = \frac{P}{v \cdot h \cdot t} \quad (2.1)$$

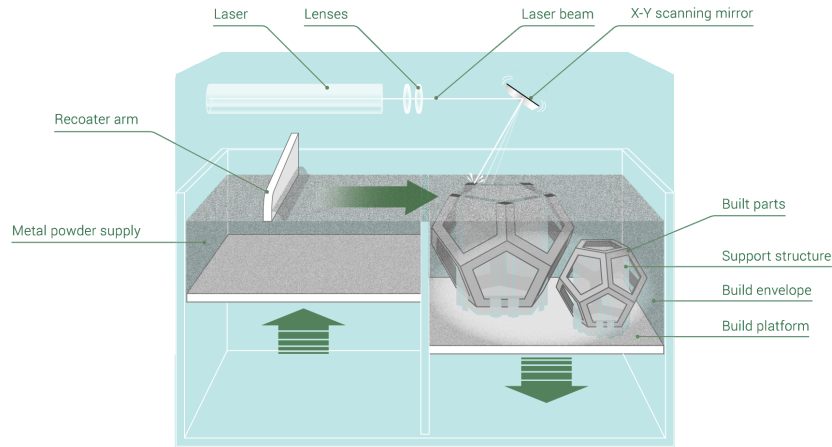


Figure 2.3: Selective Laser Melting Process[7]

These parameters have influence on the properties of the final product, such as the hardness, microstructure and residual stresses. Because of high temperature gradients during the process, a martensitic microstructure with elongated grains develops. There is also a chance of the formation of micropores in the material, which can act as nucleation sites for fatigue cracks. Therefore the SLM process is usually followed by a post-build heat treatment, that gives a better control of the microstructure and micropores in the material. Two other disadvantages of the SLM production process are the size restriction of the final part to the building platform of the machine, and the relative low production speed.

2.3 Meta-materials

Meta-materials are materials that derive their properties (mechanical, optical, electric) from their structure rather than its chemical composition (base material). This yields materials with unusual properties such as negative poisson ratio, specific refractive indexes, and very low densities. Meta-materials are usually associated with optical properties but due to development of new production methods such as additive manufacturing which enables fabrication of new structures, there is a shift to mechanical meta-materials.

Porous biomaterials can be considered as meta-materials because they derive their mechanical properties from the structure that it is made of [9]. A porous biomaterial is characterized by its unit cell type, the size of the unit cell and relative density or porosity. The unit cell can be seen as the building block that the structure is made of by repeating this cell in different directions. There are many different unit cells from which a structure can be built, with different symmetries and complexities. Some examples can be seen in Figure 2.4.

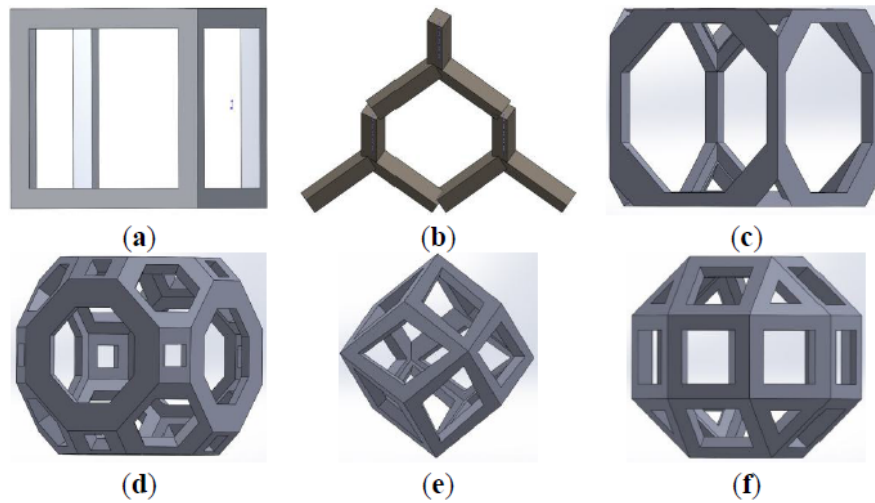


Figure 2.4: Schematic drawings of unit cells used in porous structures: (a) Cubic; (b) Diamond; (c) Truncated cube; (d) Truncated cuboctahedron; (e) Rhombic dodecahedron; (f) Rhombicuboctahedron.[9]

The size and strut thickness of these unit cells will change the overall density of the part. This can be described with different terms, such as the relative density, porosity or volume fraction. The porosity value is a percentage of the volume of the sample that is not occupied in comparison to the macro volume. The relative density and volume fraction are the opposite of porosity, and give the percentage of material compared to the macro volume. Mechanical properties such as the elastic modulus, yield stress, energy absorption and fatigue strength can be altered by varying the unit cell types and porosity. Porous biomaterials can therefore also be named as meta-biomaterials.

2.4 Fatigue theory

Fatigue is a failure mechanism of materials that are exposed to cyclic loads, usually below the yield strength of the material. The fatigue life of a material is the period between the start of cyclic loading until failure. It is usually divided into a crack initiation period and a crack growth period, because of the different factors that influence the fatigue behavior. A fatigue cycle can be characterised with a wave shape, minimum and maximum stress. From these values, the stress ratio R , mean stress and stress amplitude can be calculated. A typical fatigue cycle with a sinusoidal wave shape is displayed in Figure 2.5.

2.4.1 Crack Initiation

The crack initiation period starts with a process called cyclic slip. This is microscopic plastic deformation along crystallographic slip planes of a small number of grains located at the material surface, because of their low constraint. Subsequent slip along the same plane due to continuous cyclic loading creates slip bands, which eventually leads to crack nucleation. Surface roughness and

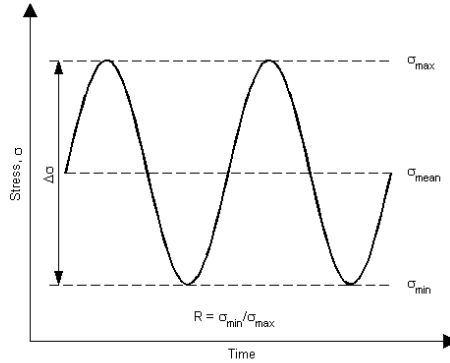


Figure 2.5: Standard Fatigue cycle description [10]

holes or notches create an inhomogeneous stress distribution in the material which increases the process of crack initiation. This period can therefore be seen as a material surface phenomenon. After crack nucleation, a microcrack slowly grows until its growth rate is not any more affected by the surface conditions. The growth rate of microcracks is very low and can cover a very large part of the total fatigue life.

2.4.2 Crack growth

The second phase of the total fatigue life is the crack growth phase. The crack growth resistance is a bulk material property and can be characterized by the crack growth per cycle as a function of the stress intensity factor K . The stress intensity factor K gives the magnitude of the elastic field in the vicinity of a crack with length $2a$, and is given by equation 2.2.

$$K = \sigma\sqrt{\pi a} * f(a/W) \quad (2.2)$$

The second part of the equation ($f(a/W)$) depends on the geometry and is a function of the crack length $2a$ and specimen width W .

The crack growth period can be divided into three regions as a function of ΔK . The threshold region, Paris region and stable tearing crack growth region are displayed in Figure 2.6. The first region is characterized by a threshold stress intensity (ΔK_{th}), below which a crack propagates extremely slow or does not propagate. The second region is described by a power function of ΔK , which is usually the Paris equation 2.3.

$$\frac{da}{dn} = C(\Delta K)^m \quad (2.3)$$

Prediction of the fatigue crack growth rate is based on the ΔK value from which a corresponding da/dN can be derived from basic growth rate data of the material.

Porous biomaterials have very small struts and therefore only little room for crack growth. It is expected that after initiation of a crack in a strut, it will grow very fast through it, after which the strut fails and the rest of the part

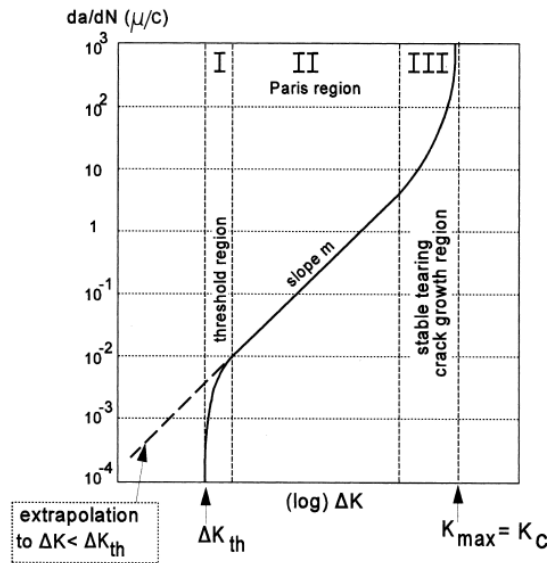


Figure 2.6: Three crack growth regions as a function of ΔK . [11]

takes over the loads. The crack growth phase is therefore only a small part of the total fatigue life of such parts and is assumed to be less important for this application.

2.4.3 Scatter

Scatter is a common phenomenon in fatigue testing. It can arise due to sample variation as a result of internal defects, surface roughness and due to imperfect control of test variables such as humidity, specimen alignment and calibration of testing machines [12] [11]. The crack initiation and crack propagation period of the fatigue life have different sources of scatter where the crack initiation period is much more sensitive to scatter. In general, scatter is highest at low stress amplitudes and becomes lower at high stress amplitudes. Scatter of the total fatigue life is primarily due to scatter of the crack initiation phase, which is small if it is easy for cracks to nucleate. This is for example valid for parts with a high surface roughness.

2.4.4 SN curves and Fatigue diagrams

One way of displaying the fatigue properties of a material, is plotting the stress amplitude or maximum stress to the amount of cycles to failure. This is called an S-N or Wöhler curve which can be obtained from fatigue tests at different stress levels. Usually these tests are performed at a constant stress ratio of $R=1$. This results in a stress amplitude that is the same as the maximum stress. An example of an SN-curve is displayed in Figure 2.7.

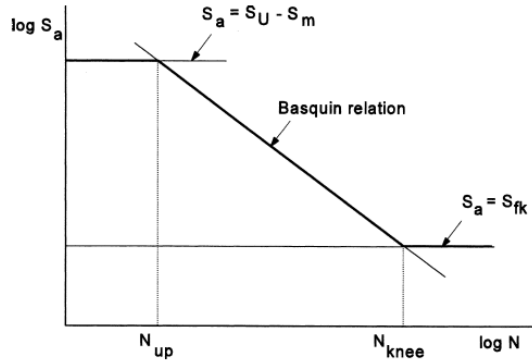


Figure 2.7: Schematic representation of a typical SN-curve [11]

Different values can be obtained from an SN-curve. A horizontal asymptote at low stress levels is the fatigue limit, which is the stress level under which a crack does not grow to failure. If the stress and amount of cycles are plotted on a logarithmic scale, usually a linear relation can be found for a range of these values. This can be written as in equation 2.4 which is known as the Basquin relation. The linear part of the SN curve has a slope of $1/k$.

$$S_a^k N = \text{constant} \quad (2.4)$$

As was showed in Figure 2.5, the ratio between minimum and maximum stress in a cycle is designated as the R-ratio. Increasing this R-ratio results in a fatigue cycle with a higher mean stress. In some cases this constant mean stress can significantly influence the fatigue life of a sample, which can be described as the R-ratio effect, mean stress effect or stress ratio effect.

Tests at different stress ratios or mean stress levels, can be combined in a single plot called a fatigue diagram. An example of such a plot and how it can be obtained can be seen in Figure 2.8. SN-curves with different mean stress levels are combined to a cross-plot with the stress amplitude as a function of the mean stress. This plot shows constant life lines that give the relation between the mean stress and stress amplitude that is allowed for a certain number of cycles. All points below such a line are considered safe and will not result in failure. The effect of R-ratio, especially for the crack growth phase has been proved to be very material dependent([10], [13]).

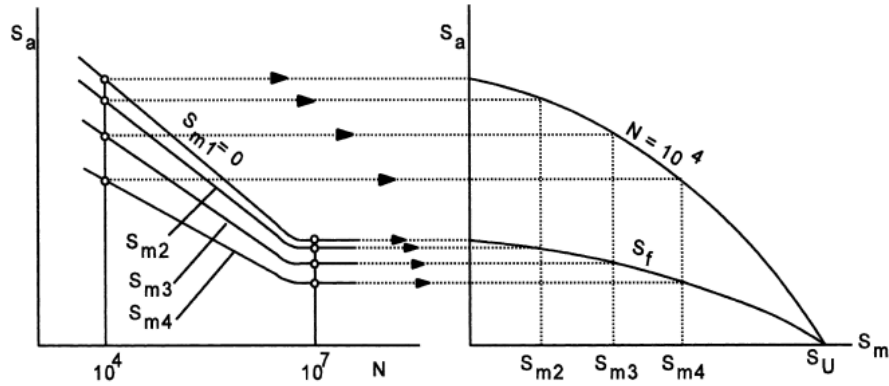


Figure 2.8: Fatigue diagram derived from different S-N curves. [11]

Fatigue diagrams are mentioned under different names in the literature, such as constant life diagrams, Goodman diagrams or Haigh diagrams. The last two names come from different formulas to fit the data from fatigue diagrams. Originally fatigue diagrams were used as design curves to determine the maximum allowable stress amplitude at a given mean stress, for a constant number of cycles.

The Goodman equation originates from the dynamic theory, which states that vibratory loads produce the same effect on a material as a suddenly applied load and are considered to produce the double amount of stress as if applied slowly. As a consequence, the sum of the mean stress and twice the alternating stress must be lower than the ultimate strength of the material. This equation was not consistent with experimental data, resulting in an adjustment of the Goodman relation by changing the ultimate stress with the fatigue life at $R=1$ which is fully reversed loading. The new equation is called the Modified Goodman equation(2.5).

$$\sigma_a = \sigma_{-1} \left(1 - \frac{\sigma_m}{\sigma_u} \right) \quad (2.5)$$

The alternative equations to describe the mean stress behavior are primarily created to better match the experimental data. This is for example the parabolic Gerber equation (2.6), which for most materials turned out to be more conservative than the Modified Goodman equation[12].

$$\sigma_a = \sigma_{-1} \left[1 - \left(\frac{\sigma_m}{\sigma_u} \right)^2 \right] \quad (2.6)$$

Two examples of fatigue diagrams with data that fit the Goodman and Gerber parabola are displayed in Figure 2.9. High cycle fatigue tests of aluminium and steel fall both between the region of these formulas.

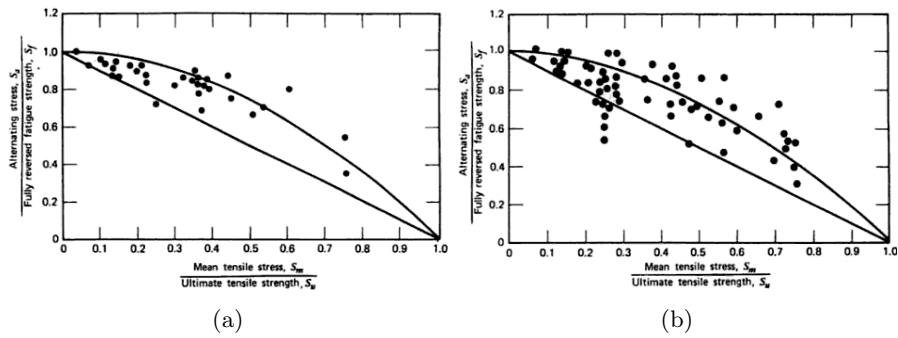


Figure 2.9: Typical constant life diagrams with Goodman and Gerber parabola with representative data of steel ($\sim 10^7$) cycles (a) and Aluminium ($\sim 5 \cdot 10^7$ cycles)(b) [13]

One equation that is important to mention because of its good fit with Ti-6Al-4V fatigue data, is the Jasper equation(2.7). This formula is based on the theory that the fatigue life is related to the stored energy density range per cycle, that could be written as $U = \frac{1}{2E}(\sigma_{max}^2 \pm \sigma_{min}^2)$. The Jasper equation can then be derived resulting in an expression of the alternating stress in terms of the stress ratio R (2.7).

$$\sigma_a = \frac{\sigma_{-1}}{\sqrt{2}} \sqrt{\frac{(1-R)^2}{1-R|R|}} \quad (2.7)$$

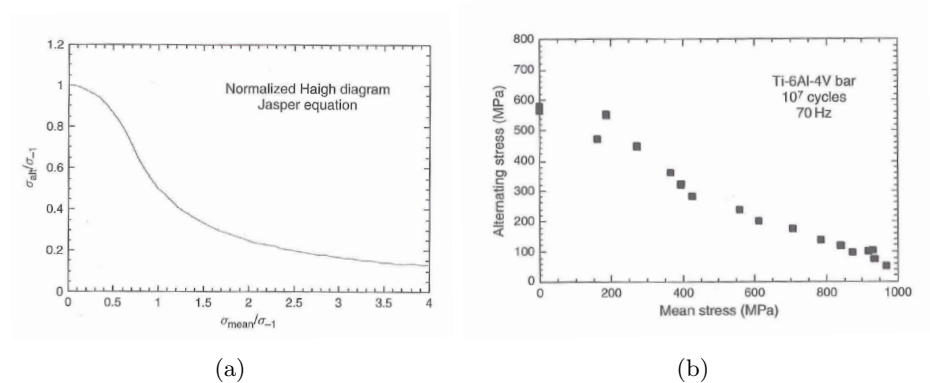


Figure 2.10: Jasper equation on normalized Haigh diagram (a) Haigh diagram of Ti-6Al-4V bar (b) [14]

Figure 2.10 shows the normalized Jasper equation with fatigue data that is obtained from Ti-6Al-4V bar material. It can be seen that the general shape is the same for both curves. A downside of the Jasper equation is that the whole curve is based on only a single parameter σ_{-1} . It is therefore not possible to accurately compare this equation with test data that does not include this stress ratio.

All equations mentioned above are based on fatigue data in tension or reversed (tension-compression) in the case of $R=-1$. The constant life diagrams

do not describe the effect of a compressive (negative) mean stress. Generally a compressive mean stress is very beneficial for the fatigue life, and experimental data showed that the modified Goodman equation could be extrapolated into this region.

2.5 Fatigue behavior of Ti-6Al-4V and slm Ti-6Al-4V

2.5.1 Ti-6Al-4V

Ti-6Al-4V is the most common titanium alloy. It is used in more than 50% of the applications of titanium. The aerospace industry accounts for almost 80% of the use of Ti-6Al-4V. The second largest application field is in biomedical prostheses, which accounts for 3% of the usage. The reason that Ti-6Al-4V is so widely used is its unique properties. It has a high specific strength, good corrosion and fatigue properties, and more specific for biomechanical applications, a low modulus and biological compatibility. Titanium is an $\alpha + \beta$ alloy, meaning that it has two phases. The α phase has an hcp (hexagonal close packed) structure, which is stable at temperatures below 883°C. At higher temperatures, the bcc (body centered cubic) β phase becomes stable. Alloying elements in titanium can stabilize the α phase by increasing the transition temperature. Examples of α stabilizers are aluminium, oxygen and nitrogen. Elements as vanadium, iron and hydrogen are β stabilizers, which decrease the transformation temperature. At room temperature, Ti-6Al-4V consists of about 90 vol% α -phase, which therefore dominates the properties of this alloy. Aluminium in Ti-6Al-4V increases the strength of the titanium by solid solution hardening. The main function of vanadium as alloying element is stabilizing the β phase, which is also beneficial for the strength of the material.

Ti-6Al-4V is available in several grades. One grade that is important to mention because of its application in biomechanical implants, is the extra low interstitial grade (ELI). For this grade, the interstitial element oxygen is held below 0.13wt%, which is normally around 0.2wt%. Higher amounts of oxygen and nitrogen decrease the ductility and toughness, making the material more brittle [15].

Also the microstructure has a large influence on the mechanical properties of Ti-6Al-4V. There are some standardized heat treatments to create microstructures for different applications. Examples of what can be achieved by changing the microstructure are increased machineability, optimal fracture toughness and variations in ductility. Because of the two phases that are present in Ti-6Al-4V, there are two microstructure compositions that can be created, which are lamellar and equiaxed with either fine or coarse grains. Examples of lamellar microstructures that result from furnace cooling and quenching from different start temperatures are displayed in Figure 2.11. Fine grain microstructures generally have an increased strength and ductility and are able to retard crack nucleation. Coarse microstructures are more resistant to crack growth, so a general conclusion that can be drawn regarding grain size for maximum fatigue resistance, is to have small grains at the surface and larger grains in the interior [16]. The equiaxed microstructures have a high ductility and fatigue strength and a lamellar microstructure has a higher fracture toughness and better resistance to

creep and crack growth. Bi-modal microstructures consist of both lamellar and equiaxed grains and can therefore be used to combine the advantages of both microstructure types. Equiaxed or bimodal microstructures are obtained by a recrystallisation process. Examples of equiaxed and bimodal microstructures are displayed in Figure 2.12.

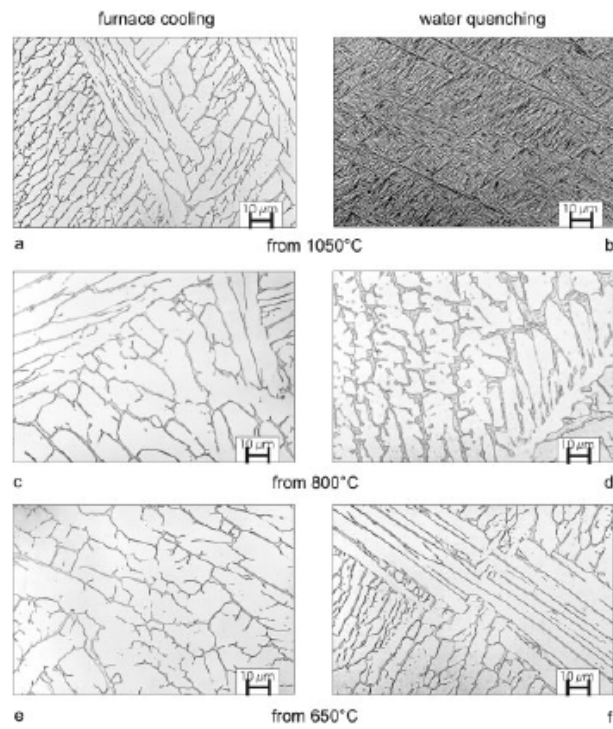


Figure 2.11: lamellar and martensitic microstructures of Ti-6Al-4V quenched from different temperatures [15]

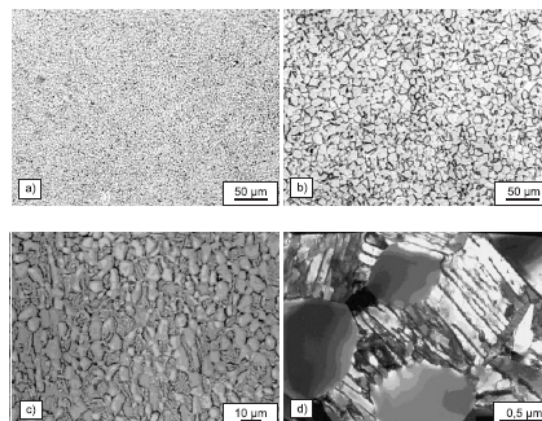


Figure 2.12: fine equiaxed(a,b), course equiaxed(c) and bimodal(d) microstructures of Ti-6Al-4V[15]

2.5.2 Fatigue behavior of Ti-6Al-4V

In order to get a better understanding of the fatigue behavior of titanium, and more specifically Ti-6Al-4V, some fatigue curves regarding crack growth, mean stress behavior and microstructural behavior are discussed.

Effect of microstructure and texture

The effect of microstructure on the fatigue life of Ti-6Al-4V is displayed in Figure 2.13a. From this Figure can be seen that the fatigue strength is much lower for coarse grains, and equiaxed microstructures perform a bit better than lamellar microstructures.

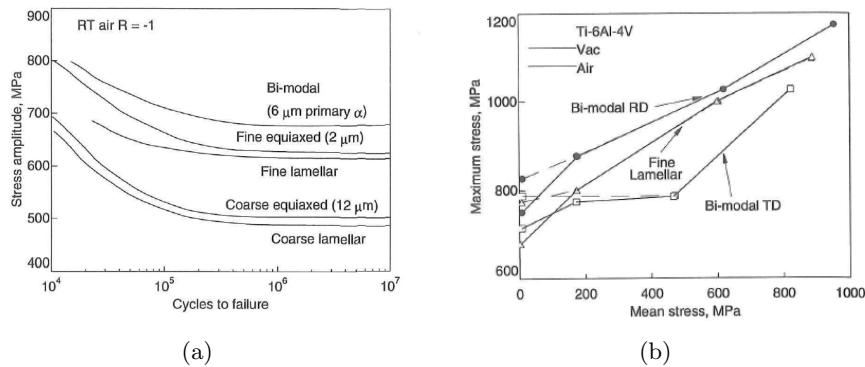


Figure 2.13: Effect of microstructure on fatigue life(a) mean stress behavior at high cycle fatigue (10^7 cycles)(b) [17]

The effect of microstructure and testing direction on the high cycle mean stress behavior of Ti-6Al-4V is displayed in 2.13 b. The Ti-6Al-4V alloy is produced by rolling and is therefore tested in the rolling and transverse to the rolling direction. A non linear mean stress behavior is observed for a bi-modal microstructure that is tested in transverse direction (TD), while this behavior is not seen in the rolling direction(RD). No clear explanation for this behavior was found.

Growth behavior

Figure 2.14 shows general fatigue crack growth behavior of Ti-6Al-4V with increasing load ratio. Although the crack growth period is expected to be very short in the application of porous biomaterials, it is important to mention that the the effect of R-ratio is highest in the first stage of crack growth with increasing stress ratio. This means that the threshold value for constant crack growth is lower, so smaller cracks are expected to propagate, but at the same rate as for lower stress ratios.

The study of Caton et al. [19] showed a small effect of the stress ratio on the crack growth rate. After testing cylindrical specimens with milled micro-notches at stress ratios of 0.5, 0.1 and -1 it was found that a low mean stress for a given maximum stress resulted in faster crack growth. This is in compliance with the common theory that the stress amplitude has much more effect on the

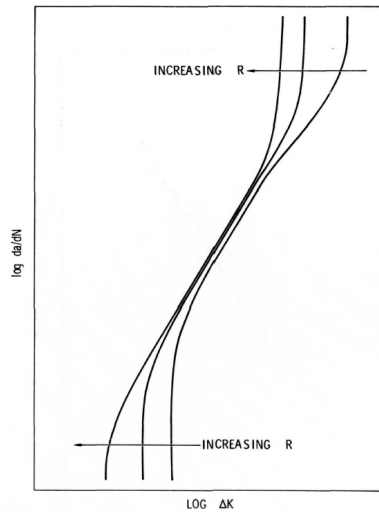


Figure 2.14: $da/dn \Delta K$ curve behavior as a function of increasing R [18]

stress fatigue life than the mean stress. This behavior is also confirmed by Ding et al. [20], where the effect of stress ratio and temperature on crack growth is investigated in Ti-6Al-4V.

Mean stress behavior

The mean stress sensitivity of $\alpha + \beta$ alloys is studied by Lindemann and Wagner [21]. An anomalous mean stress sensitivity is observed for the $(\alpha + \beta)$ alloys Ti-6-7 and Ti-5-2.5, which means that their fatigue strength at low (tensile) mean stress can be significantly lower than the linear Modified Goodman equation approximates. Ti-6Al-4V with β -annealed fully lamellar microstructure exhibits a normal mean stress dependence (linear) while fully equiaxed or duplex microstructures showed an anomalous mean stress sensitivity (AMSS). No other studies were found that confirm the behavior of this specific microstructures.

Experiments were conducted by Morrissey et al. [22] to determine the effects of test frequency and stress ratio on the high cycle fatigue behavior of Ti-6Al-4V. Three different stress ratios (0.1, 0.5 and 0.8) were tested at different frequencies (70Hz, 400Hz and 1800Hz). At low stress ratios, the fatigue strength increased with increasing frequency. This behavior continued for higher R values, until a transition zone was reached at around $R=0.8$. According to the writers, this could be a result of the strain rate effect. A strain rate effect is observed when for a constant value of strain, the flow stress (stress to maintain plastic flow) increases with increasing strain rate. Higher frequencies require higher loads to produce the same strain range, which could lead to plasticity at high stress ratios. Another observation from this study was an increase in scatter of the cycles to failure for higher stress ratios.

Another study by Morrissey et al. [23] showed that there is a transition of the high cycle fatigue behavior at stress ratios above 0.7. Strain accumulation and necking was observed at the specimens tested at high stress ratios, which is similar to the deformation of normal tension tests. The deformation of the

samples was closer related to the number of cycles than to the testing time, which corresponds with the previous mentioned research, that there is no frequency dependence of the fatigue behavior at very high stress ratios.

Figure 2.15a shows the mean stress behavior of a Ti-6Al-4V alloy with different notch-factors from circumferentially V-notched specimens. The R-ratios tested were -1, 0.1, 0.5, 0.65 and 0.8. A step loading technique was used to generate the points on the diagram. It can be observed that an increase of the notch factor results in more deviation from the Goodman curve, resulting in a lower mean stress dependence of the fatigue life. Figure 2.15b shows a fatigue diagram from a fatigue test performed between 10-15Hz. Four stress ratios that were tested are -1, 0.01 and 0.5 and 0.85. The tests are performed with a maximum stress that is fixed at 0.2% proof stress ($\sigma_{0.2}$). The fatigue strength was taken at 10^7 cycles. The fatigue strength deviates from the modified Goodman line at stress ratios of 0.01 and 0.5 resulting in a low mean stress dependence. This behavior occurred for both room temperature and low temperature tests, while the R=-1 and R=0.85 values are much closer to the modified Goodman predictions. Hourglass shaped test specimens were used for these fatigue tests.

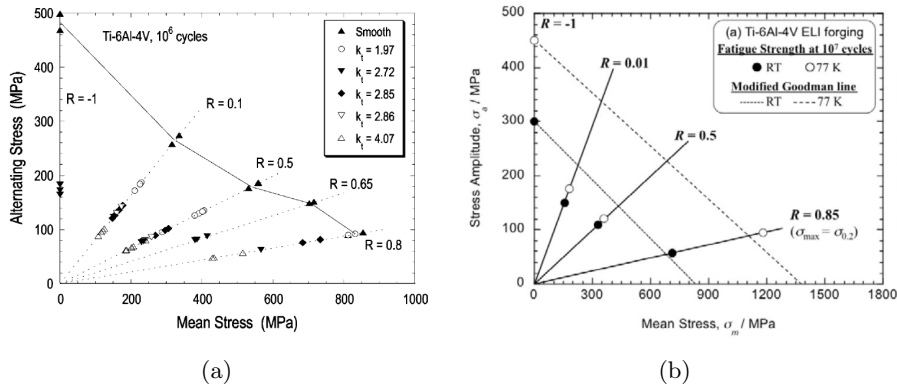


Figure 2.15: Haig diagram showing the effect of notches on the mean stress behavior. (a)[24] Effect of notches on the mean stress behavior (b) [25] Effect of temperature on mean stress behavior

Constant life diagrams of Ti-6Al-4V can be found in different fatigue data reference books. A few curves from the ASTM Fatigue data book of light alloys are displayed below and will be shortly discussed.

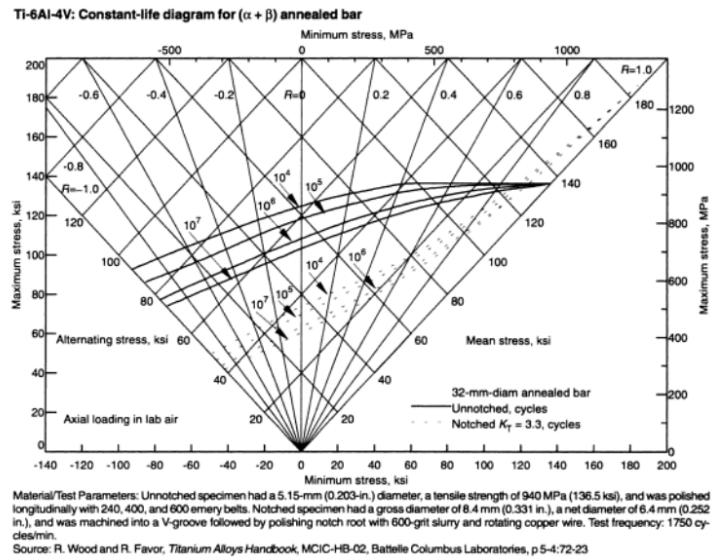


Figure 2.16: constant life diagram Ti-6Al-4V bar[17]

The constant life diagram for Ti-6Al-4V ($\alpha + \beta$) annealed bar is displayed in Figure 2.16. This Figure consists of constant life lines for both positive and negative stress ratios, which are marked as straight lines between the alternating and mean stress axes. Test results from unnotched specimens are displayed as solid lines, and notched specimens are indicated with dashed lines. What can be seen from this Figure, is that all unnotched constant life lines show the same trend. The lines are almost parallel and start to converge between $R=0.4$ and $R=0.6$ to the maximum mean stress. The behavior of notched specimens is also similar for all constant life lines, but has a more convex shape compared with the unnotched specimens, which means that the stress amplitude has more influence on the fatigue life than the mean stress. The unnotched constant life lines are slightly parabolic, indicating that they could be approached with the Gerber equation. The notched curves show a trend which has more similarities with the Jasper equation that is described earlier.

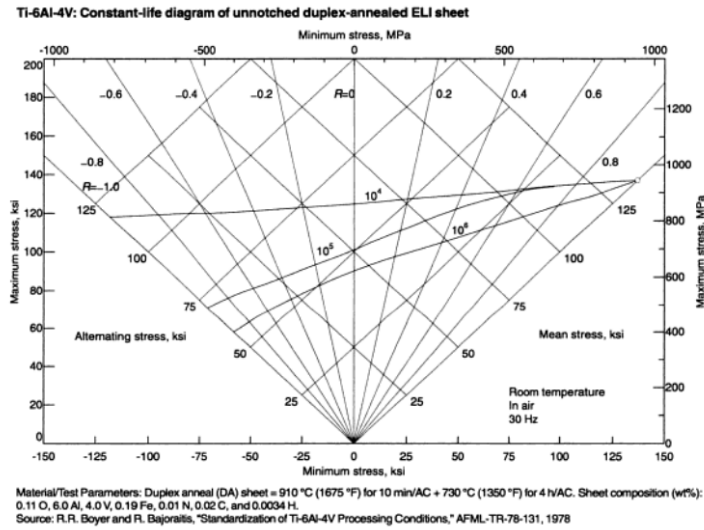


Figure 2.17: constant life diagram Ti-6Al-4V ELI[17]

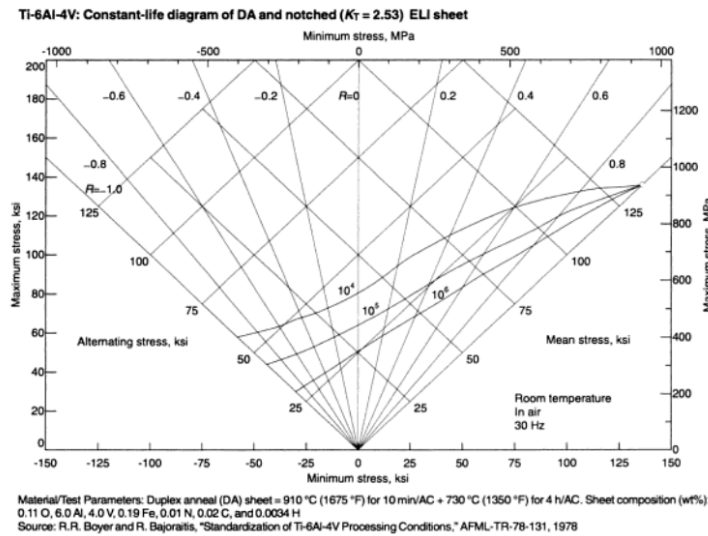


Figure 2.18: constant life diagram Ti-6Al-4V ELI[17]

The Figures 2.17 and 2.18 show the mean stress behavior of duplex annealed ELI Ti-6Al-4V, where 2.17 displays the unnotched and 2.18 the notched behavior. It can be seen that the unnotched specimens show a bigger decline of the alternating stress with increasing mean stress when compared with the notched samples. Comparing these figures with Figure 2.16, shows that Ti-6Al-4V behaves similar to the ELI Ti-6Al-4V, except for 10^4 cycles, which is fully linear in the case of the ELI Ti-6Al-4V.

Surface treatments

Surface treatments like polishing or shot peening can be used to increase the crack nucleation phase. Ti-6Al-4V is known to be very notch sensitive[3]. Therefore the various surface treatments have a large influence on the total fatigue life, which can be seen in Figure 2.19. Shot Peening (SP) creates compressive stresses on the surface of the sample, which increases the fatigue strength of an electropolished (EP) sample. A stress relieving heat treatment (SR) after shot peening reduces the fatigue strength, which could be restored by additional electropolishing. Other surface conditions like surface roughness can reduce the fatigue limit up to 40% in comparison to smooth specimens.

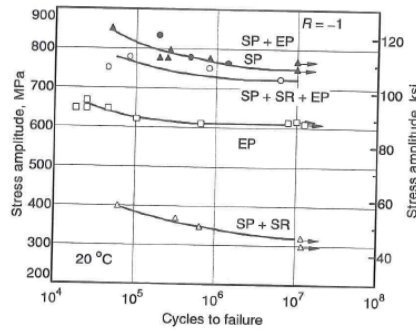


Figure 2.19: Effect of surface treatments on the fatigue behavior of Ti-6Al-4V [17]

2.5.3 Fatigue behavior of Ti-6Al-4V produced by selective laser melting

Several studies have been done on the fatigue behavior of Ti-6Al-4V that is produced by selective laser melting. Different factors that influence the fatigue behavior are investigated, such as the effect of heat treatments, build orientations and production parameters.

The fracture toughness and crack propagation of SLM components is studied by Van Hooreweder et al. [26]. SLM produced parts are compared with vacuum arc remelted (VAR) mill annealed standard oxygen Ti-6Al-4V. The microstructure of the SLM produced parts consist of fine acicular α' -martensite with sharp needles. All tests are performed with Compact Tension-specimens. The fine grained martensitic structure tend to slow the propagation of small cracks due to the high density of grain boundaries that act as obstacles for the crack growth. For cracks larger than 1mm, this effect is reversed and the crack propagation speed is increased. In general, the SLM Ti-6Al-4V shows inferior fracture toughness when compared to the VAR material. This could be a result of the increased brittleness of the martensitic microstructure. The crack growth rates on the other hand showed more acceptable values because of the high density of grain boundaries.

Leuders et al. [27] did a research on the effect of the microstructure on the fatigue behavior of Ti-6Al-4V manufactured with SLM. Also the effect of heat treatments is investigated. Four different samples were tested. One as-built,

one heat treated at 800 degrees,(below the β -transus temperature), one heat treated at 1050 degrees (above β -transus) and one hot isostatic pressed (HIP). The initial microstructure and the effect of the different heat treatments are displayed in Figure 2.20. It can be seen that the heat treatment at 800°C did not result in major changes in the microstructure. The HIP and 1050°C heat treatments resulted in substantial grain growth, and changed the microstructure into more equiaxed grains. The geometry of the specimens were cylindrical for high cycle fatigue testing, and Compact Tension(CT) specimens were made for fatigue crack growth tests. Residual stresses and micropores that are present due to the Selective laser melting process did not have a strong impact on the tensile properties but had a large effect on the fatigue behavior. Stress concentrations at the micropore defects significantly reduced the fatigue strength, mainly in the fatigue initiation phase. The HIP treatment increased the ductility of the material which resulted in better fatigue properties that are close to conventionally processed Ti Alloys. Crack growth can also behave similar to conventionally processed Ti-6Al-4V by stress relieving heat treatments at lower temperatures, without changing the microstructure.

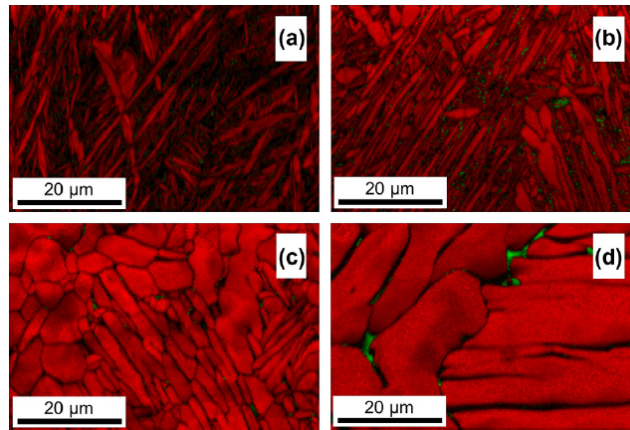


Figure 2.20: Microstructure of Ti-6Al-4V directly after production(a), after 2h at 800°C(b) HIP treatment (c) and 2h at 1050°C (d) [27]

The fracture toughness and crack growth rate of Selective Laser Melted Ti-6Al-4V is also studied by Cain et al. [28]. Specimens from grade 5 Ti-6Al-4V powder are produced with three different build orientations and two heat treatments are compared. A Stress relieve treatment at 640°C for two hours, and annealing treatment at 890°C for two hours is applied. The microstructure of the as-built samples consists of martensitic fine α' plates. The stress relieve treatment partially decomposes towards acicular α and the annealing treatment forms the Widmanstätten α/β structure. Both heat treatments improve the fracture toughness and fatigue crack growth resistance. The effect of different build orientations was most evident in the the samples without heat treatment, while the fracture toughness values of the three orientations increased and were almost the same after the treatments. The tensile properties are less influenced by the specimen build direction. The tensile strength and yield strength are substantially reduced after the heat treatments.

Biomaterials produced with SLM

Previous research focused on the general fatigue behavior of porous biomaterials that are build up from different unit cells, with different porosity values. A short summary of these studies is given, together with the main conclusions that have been drawn.

The fatigue behavior of porous structures made of Ti-6Al-4V ELI powder (ASTM B348 grade 23) using SLM is studied by Amin Yavari et al. [29]. Four different porous structures were manufactured with variations in porosity by changing the strut size and pore size. Fatigue tests were carried out at 15Hz, with a constant load ratio of $R=0.1$. Eleven different load values were chosen such that the maximum stress levels were between $0.2\sigma_y$ and $0.8\sigma_y$. The samples are assumed to have failed when the stiffness dropped more than 90%. The fatigue life for more porous structures is much shorter, but the normalized fatigue S-N curves are very similar as can be seen in Figure 2.21. The unit cell

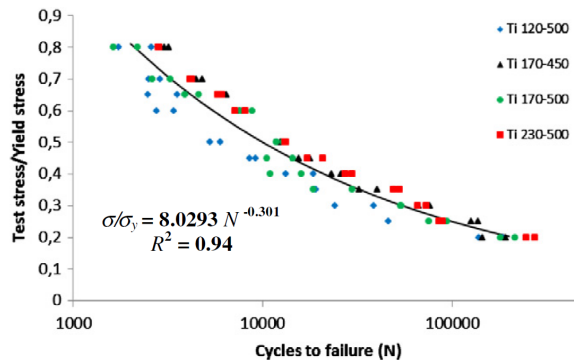


Figure 2.21: Normalised fatigue diagram of dodecahedron unit cell porous structures with different porosity values [29]

of all porous structures in this study is dodecahedron. Porosity measurements are performed for five samples of each series. The porosity is determined by dry weighing and Archimedes measurements.

The static mechanical and (compression) fatigue properties of three different unit cell structures were also tested by Amin Yavari et al. [30]. The unit cells that are used are cube, diamond and cuboctahedron. The fatigue tests are performed at 15Hz and with a stress ratio of $R=0.1$. The fatigue properties proved to be highly dependent on the type of unit cell and porosity. Results of the fatigue tests with the diamond unit cell specimens are displayed in Figure 2.22. The cube unit cell did not fail after 10^6 cycles. This because the vertical struts are loaded in pure compression, under which cracks do not grow. The other unit cell types showed lower fatigue lives with increasing porosity. The normalized SN curves of the three unit cells are displayed in Figure 2.23. It can be seen that the fatigue limit of porous structures based on the truncated cuboctahedron and diamond unit cells are much higher than porous structures based on the rhombic dodecahedron unit cell.

This study also introduces the term "meta-biomaterials", which can be assigned to the newly developed porous structures that are produced with SLM.

Compression-compression fatigue tests by Hrabe et al. [31] at 15Hz and

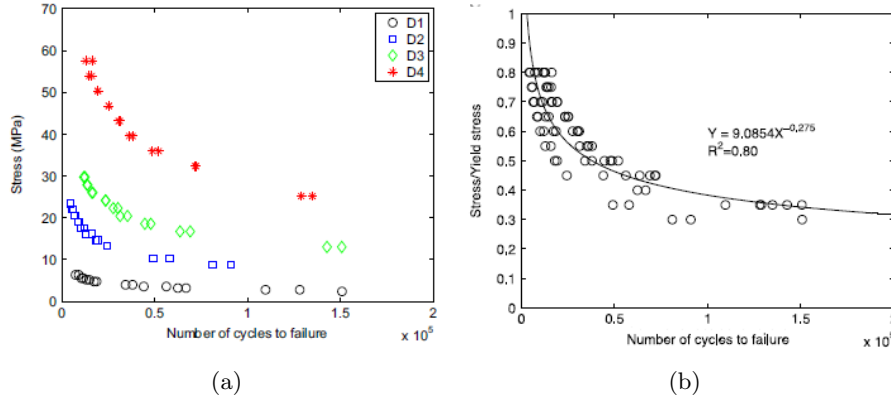


Figure 2.22: SN curves of diamond unit cells with different porosities (a) Normalized SN curves of different porosity diamond unit cells(b) [30]

$R=0.1$ resulted in normalized fatigue strengths at 10^6 cycles ranging from 0.15 to 0.25, which is lower than the expected life of 0.4 based on solid material with the same microstructure. The structures are built-up from diamond unit cells and are produced with selective electron beam melting (EBM). The reduced fatigue life could be a result of stress concentrations from closed porosities, stress concentrations due to the large temperature gradients during manufacturing and the microstructure consisting of acicular α or martensite. The samples had relative densities between 0.17 and 0.40, achieved by varying the pore and strut size. The pore size is altered by scaling of the CAD file, while the strut size was affected by the energy input. The fatigue failure of the samples showed a clear fracture plane at 45 degrees to the loading plane. Multiple strut fracture surfaces, all oriented parallel to the compressive force axis showed extensive secondary cracking at strut nodes and relatively little plastic deformation of the struts was observed. SEM imaging showed multiple internal porosities in the material, which can lead to stress concentrations that reduce the fatigue life. Striations-like markings were also visible, indicating cyclic crack growth.

The study of Campoli et al. [32] compares the mechanical properties of open cell titanium biomaterials with Finite Element models. The FE models are implemented with manufacturing irregularities such as variations in strut diameters. The SLM manufactured titanium test samples are built-up from the rhombic dodecahedron unit cell. From this paper is concluded that FE models can accurately predict the properties of porous biomaterials manufactured using SLM. The FE models are also more accurate than analytic models in predicting the mechanical properties. The structural irregularities caused by the manufacturing process must be implemented in the FE model because they significantly influence the mechanical properties.

The mechanical properties of SLM manufactured diamond unit cell titanium structures are determined by Ahmadi et al. [33]. The experimental results were compared with FE models and analytic solutions. Solid cylindrical samples were also produced with SLM and used to determine the mechanical properties of the Ti-6Al-4V material. Porous samples with four different strut length to strut diameter ratios resulting in four different porosity values were tested

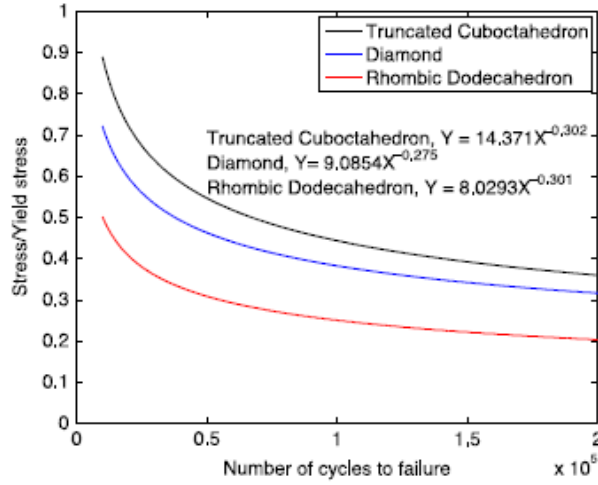


Figure 2.23: Normalized fatigue curves of biomaterials based on three different unit cell types[30]

to determine the mechanical properties of the porous metals. A summary of the mechanical properties of the diamond unit cell structures can be found in table 2.3. The analytic and numerical solutions are in good agreement with experimental results for small apparent density (AD) values (large porosity). For large AD, the analytic results based on the Euler-Bernoulli beam theory significantly deviate from the experimental results, while the Timoshenko beam theory values are relatively closer to the experimental observations.

Table 2.3: Mechanical properties of diamond unit cell structures [33]

AD	Porosity [%]	σ_{pl} [MPa]	$E_{\sigma_{20}-\sigma_{70}}$ [GPa]
0.36	64	99.64	4.24
0.265	73.5	62.92	2.64
0.181	81.9	25.27	1.22
0.105	89.5	8.20	0.37

Wauthle et al. [34] studied the effect of build orientation and heat treatments on the mechanical properties of additively manufactured diamond lattice structures. The structures had a relative density of 0.3 which is equal to 70% porosity. Five different samples by variations in build orientation and unit cell orientation were created, and the effect of a stress relieve and HIP treatment were investigated. The orientation of the unit cell did not have an influence on the mechanical properties, while the build orientation variations resulted in a decrease of the yield and maximum stress of around 35%. The heat treatments had similar effects on the mechanical properties, independent of the build orientations. A stress relieve treatment increases the yield stress and the HIP treatment decreases the maximum strength without major changes of the yield strength. Both heat treatments resulted in a stiffness increase of around 20%.

The studies of Brenne et al. [35] and Gorny et al. [36] investigated the mechanical properties of cellular structures and the effect of their microstructure.

They used Digital Image Correlation (DIC) to look at the local strains during cyclic and static loading conditions. The research of Brenne et al. [35] used a conventional digital camera equipped with a macro lens to obtain images, which were then processed with the commercial DIC software package VIC-2D. The study of Gorny et al. [36] used a Scanning Electron Microscope that was equipped with a miniature loading frame to obtain images during the compression test. Also this research used VIC-2D software to process the images. The obtained strain distributions are displayed in Figure 2.24. Both images show a clear failure line of 45 degrees with respect to the loading direction. This failure mode was also found in the studies of Li et al. [37] Cheng et al. [38] and Cansizoglu et al. [39] which are all studies on the compression behavior of Ti-6Al-4V mesh arrays fabricated by EBM.

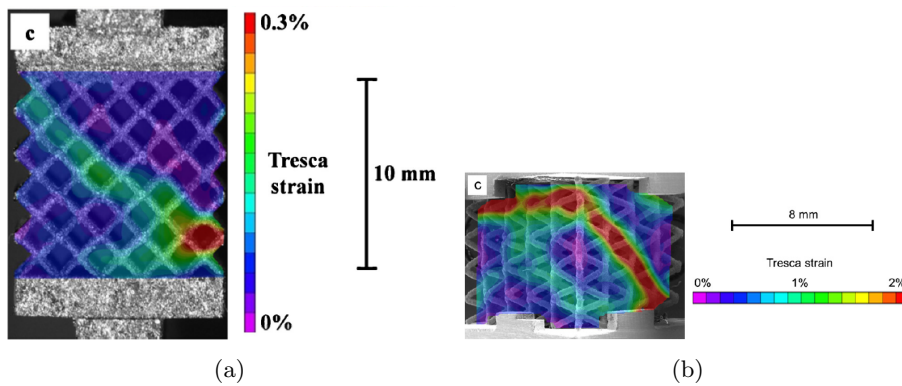


Figure 2.24: Local strains at half of the total fatigue life from [35](a) local strains during compression test from [36](b)

2.5.4 Meta-biomaterial

The development of porous biomaterials by additive manufacturing has led to new designs of meta-materials that cannot be made with conventional production techniques. These new designs must be tested before any practical application is possible. As described in section 2.3, meta-materials can be considered a structure on a small scale, but are treated as a material regarding their mechanical properties, by appointing values such as yield strength and elastic modulus to it. Fatigue test to create SN-curves are also associated with material properties instead of structures which raises the question if the results are comparable to the bulk material properties. It has already been shown that the SN curves of porous biomaterials show good compliance with bulk material, but no tests at different stress ratios have been performed. Therefore for this research, the R-ratio behavior of meta-biomaterials will be investigated. Two different sample types, one with a very high and one extremely low porosity value will be tested. In this way, the behavior of a very porous and almost solid sample can be compared to investigate what determines the R-ratio behavior of meta-biomaterials.

Chapter 3

Materials and Methods

This study is aimed at looking at the R-ratio influence on fatigue for SLM produced meta-biomaterials. To test the fatigue behavior, samples with two different porosity values are produced. This is followed up by two morphological characterization methods after which a static mechanical test is performed to determine the mechanical properties. Finally fatigue tests at different R-ratios are carried out, and an experimental DIC method is used to give more insight in the deformation behavior during fatigue.

3.1 Materials and manufacturing

Test samples are manufactured using Selective Laser Melting (Layerwise) from Ti-6Al-4V ELI powder according to ASTM B348, grade 23. This alloy has a theoretical density of 4.42 gcm^{-3} . The samples are build using the same procedure as described in previous studies [29] [30] [33] [42] [47]. They are produced in an inert atmosphere on a solid titanium substrate, from which they are subsequently removed using wire Electrical Discharge Machining (EDM).

Porous samples used for mechanical testing are built-up from diamond unit cells, from which the front view and basic building block is displayed in Figure 3.1. This is an 80% porous cylindrical sample with a diameter of 15mm and length of 20mm. Two specimen types are created by varying the strut thickness, resulting in theoretical porosities of 80% and 10% (Table 3.1).

Table 3.1: Morphological properties (Average \pm Standard deviation)

Sample name	HP80*	LP10*
Dimensions, D x L (mm)	15 x 20	15 x 20
Dry weight (g)	3.114 ± 0.079	14.84 ± 0.139
Porosity, dry weighing (%)	80.1 ± 0.5	7.3 ± 0.9
Porosity, Archimedes (%)	79.2 ± 0.6	n.A.
Porosity, Micro-CT (%)	79.8 ± 0.3	14.2 ± 0.2
Pore size, Micro-CT (μm)	765 ± 112	209 ± 76
Strut size, Micro-CT (μm)	306 ± 60	724 ± 179

* Theoretical porosity based on sample design

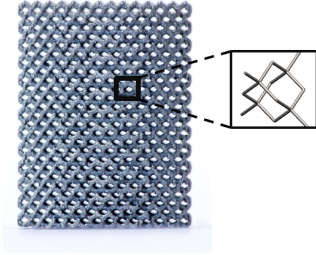


Figure 3.1: Diamond unit cell porous structure, Dimensions: 15x20mm

3.2 Morphological characterization

After production by Selective Laser Melting, a verification is needed to check if the samples comply with the designed porosity value. For this research, the samples were characterized by Archimedes measurements and micro-CT scans. The test procedure of the Archimedes measurement is based on ASTM B311[48]. This standard describes the procedure for measuring the density of powder metallurgy materials. A batch with a minimum of five samples were first weight on a balance with a precision of 0.0001g (Denver Instruments AA-160). The 'dry porosity' was then calculated by dividing the actual weight with the theoretical weight of the macro volume. The sample was then submerged in pure ethanol and weight again, from which the actual volume can be calculated. The Archimedes porosity was then calculated by dividing this actual volume with the total macro volume of the sample.

Micro-CT scans were performed on a Caliper LifeSciences Quantum FX μ CT scanner. This is a medical purpose machine with a pixel size between $20\mu m - 128\mu m$. The samples were scanned for 120 seconds at 90kV and $180\mu A$, at a resolution of $48\mu m$ per pixel. The image processing method is similar to previous studies from [30] and a more detailed description is provided in [9]. The images were processed using the software package imageJ. This was done by first applying an automatic local threshold (Niblack, radius 15) to create a binary image. The same thresholding method was applied for all images. From this binary image, the overall porosity and average pore and strut sizes were determined using the volume fraction algorithm from the BoneJ [49] plugin. Five samples of each porosity value were scanned (Table 3.1).

3.3 Static mechanical testing

The test procedure for the static compression test was based on NEN-ISO 13314:2011 [50]. A Zwick Z100 (100kN) test system with compression plates was used for these tests. A constant strain rate of 1.2 mm/min was applied until 60% strain after which the test was automatically stopped. A total of three specimens of the high porosity were tested. The low porosity samples were tested on an INSTRON 250kN test system, because the maximum force exceeded 100kN. Only one specimen of this porosity value has been tested. From the compression tests the following data is obtained: First maximum stress (σ_{max}) and corresponding strain (e_{max}), the plateau stress (σ_{pl}) which

is calculated as the arithmetical mean of the stresses between 20% and 40% strain, the compressive offset stress (σ_{off}) which is the compressive stress at 0.2% plastic strain obtained from the quasi-elastic gradient, the quasi-elastic gradient (E_{20-70}) which is the elastic straight line between 20% and 70% of the plateau stress, and the Energy Absorption (E.A.) which is the area under the stress-strain curve up to 50% strain. The offset stress is also appointed as the yield stress for comparison with other studies. All stresses mentioned in this paper are effective stresses, based on the total circular area of the cylindrical sample with a diameter of 15mm.

3.4 Fatigue Testing

There is no test standard for compression-compression fatigue tests of porous materials. Therefore the procedure based on previous fatigue tests with porous biomaterials ([29], [30]) was used. SN curves were created with each ten data points by force-controlled fatigue testing at ten different maximum stresses between 0.2 and 0.8 times the yield(offset) stress. Each test is repeated at least two times, and if the difference between cycles to failure was larger than 40% of their average value, a third sample was tested. The fatigue tests were carried out at a stress ratio of R=0.1, R=0.3, R=0.5 and R=0.7, resulting in an SN curve for each stress ratio. An exponential fit to the SN curves was carried out using the Matlab Curve fitting tool. The SN curves were then combined to create a constant life (fatigue) diagram, which can be used to visualize the mean stress behavior of these materials and to be able to compare this with literature. A few extra tests were conducted at a stress ratio of R=0.8 to obtain more data points for constructing the constant life diagram. All tests were carried out on an MTS 100kN hydraulic test machine, at a loading frequency of 15Hz with a sinusoidal wave shape. The tests were continued until failure of the specimen, however exceeding 10^6 cycles was regarded as a run-out for this study. The run-out tests are marked with an arrow in the final SN curve.

A precise moment of failure is difficult to pinpoint in a compression-compression test where a failed specimen can continue to carry load. In this study, failure was defined by an increase in displacement of 2mm, as opposed to a stiffness drop of 90% that was used in previous fatigue studies Amin Yavari et al. [30] Amin Yavari et al. [29]. To prevent the sample from moving and making sure that the sample was aligned properly during the tests, a sample holder as displayed in Figure 3.2 was used. The specimens were placed between two of these parts.

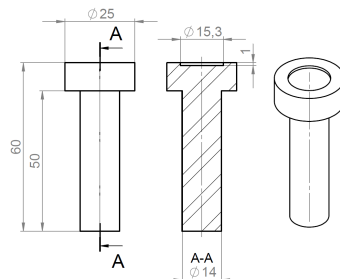


Figure 3.2: Specimen fixture for fatigue tests, dimensions in (mm)

3.5 Digital Image Correlation

During a selection of fatigue tests, pictures were taken with a Digital Image Correlation (DIC) [51] camera system (Optomotive Velociraptor) at an interval of 100 cycles. In order to obtain images at the same point in every cycle, the testing machine was programmed to stop at the maximum load after every 100th cycle, and send a signal to the camera system which then triggered the camera shutter after which the cycle continued. This process was repeated until final failure of the sample. The obtained images were processed with Matlab to visualize the local displacement or strain values of the sample. This was done by using a feature detection algorithm (Speeded Up Robust Features, *detectSURFFeatures*) from the Computer Vision System Toolbox that looks for matching features in two images. A close-up of the sample from the image correlation process is displayed in Figure 3.3. In this picture, the two compared images are placed on top of each other with the first picture in red, and the displaced picture in blue. Corresponding features are then marked with a yellow line to indicate the displacement. The distance in pixels of the two successive pictures is then calculated after which an outlier filter is applied to remove unwanted points. The distances were then converted to strains by dividing the displacement with the initial length of the sample that was measured with a calliper before each test. The final strain values were then visualized by applying a colored marker to the displaced point, ranging from blue to red with an increasing magnitude of the strain value. It should be noted that this methodology was developed specifically for this study and has not been thoroughly validated for its strain accuracy. Nevertheless, the ability to observe how the strain field changed, regardless of the accuracy of the strain magnitudes, proved to be useful for understanding the failure of the specimen.

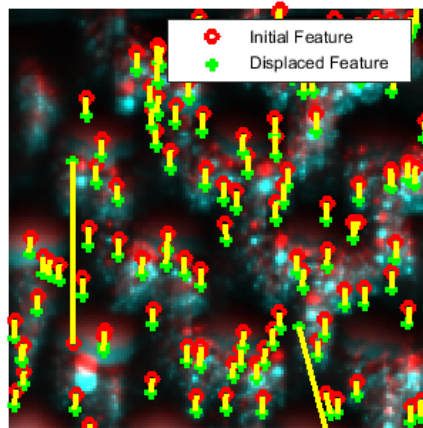


Figure 3.3: Detection of corresponding points in Digital Image Correlation code

Chapter 4

Results

4.1 Characterization

The results of the Archimedes and micro-CT experiments are displayed in Table 3.1. The low porosity samples show a large difference between the dry weighing and micro-CT measurements. An Archimedes measurement was not performed for this specimen group, because the internal closed pores would not be filled up with liquid, resulting in false measurements of the total volume. The micro-CT images showed an indication of entrapped powder from the SLM process.

4.2 Mechanical testing

The average yield stress of the high porosity samples was determined at 43 MPa and together with the other determined values, that are displayed in Table 4.1, showed a relative low standard deviation. The struts of the specimens failed close to the compression plates, either at the top or bottom, after which it gradually crushed from this location (Figure 4.1a). An angled failure line was observed during the gradual break down as can be seen in the same figure. Only a single low porosity sample could be tested as the high compression strength of the samples caused localized damage to the specimen fixture. A maximum stress of 959 MPa was reached during this test, after which the sample failed very abrupt, separating into three parts. This failed sample is displayed in Figure 4.1b. What also can be seen from this figure is the almost solid appearance. The force-displacement curve of the high porous samples is provided in appendix C.

Table 4.1: Compressive mechanical properties (Average \pm Standard deviation

Sample name	HP80	LP10*
σ_{max} (MPa)	55.6 ± 0.8	959.3
e_{max} (%)	6.3 ± 0.7	20.9
$\sigma_{off}[\sigma_y]$ (MPa)	43.0 ± 2.1	666.1
σ_{pl} (MPa)	35.3 ± 2.2	n.A.
E_{20-70} (GPa)	1.36 ± 0.46	7.91
E.A.(MJm ⁻³)	17.3 ± 0.6	n.A.

* Based on a single sample

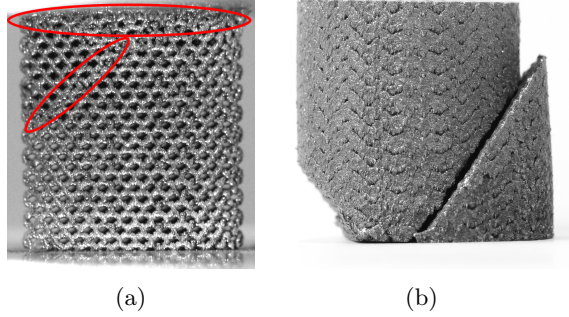


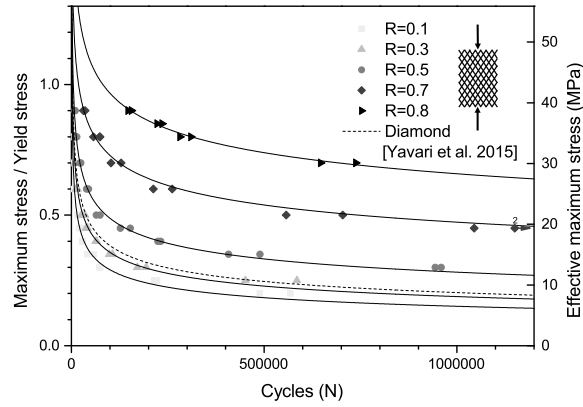
Figure 4.1: Typical sample failure at static compression of high (a) and low (b) porosity

4.3 Fatigue testing

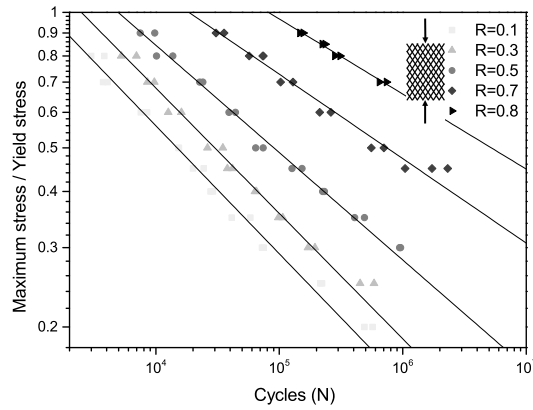
The fatigue life at five different stress ratios are plotted against the maximum stress in Figure 4.2. It can be seen that the maximum load for some tests was increased to $0.9\sigma_y$. This was done to create more points on the SN curve, because at high stress ratios, the number of cycles would exceed 10^6 at maximum stresses of $0.5\sigma_y$. The extra stresses also resulted in more comparable stress amplitudes at different mean stresses, which are useful for construction of the constant life diagram.

The dotted line in Figure 4.2a is from a previous study of Amin Yavari et al. [29], where the fatigue behavior of different unit cells, including the diamond unit cell, was investigated. The line represents the normalized fatigue test of the diamond unit cell with 80% porosity, at a stress ratio of 0.1. The line is very close to the fatigue tests from this research at a stress ratio of 0.3. The only difference with the tests of this research are the dimensions of the sample, which had an approximate length of 15mm and diameter of 10mm.

When displaying the S-N curves on a logarithmic scale as has been done in Figure 4.2b, a similar slope change is observed for stress ratios 0.7 and 0.8 in comparison to the stress ratios of 0.1 and 0.3, which seem parallel. All SN curves show a very good exponential fit, with R squared values of around 0.98. The parameters of the exponential fit are displayed in Table 4.2.



(a)



(b)

Figure 4.2: Obtained SN-curves at different stress ratios on linear (a) and logarithmic (b) scale

Table 4.2: Exponential fit parameters ($y = ax^b$)

	a	b	R^2
R=0.1	7.703	-0.2846	0.9854
R=0.3	8.848	-0.2787	0.9876
R=0.5	7.620	-0.2387	0.9880
R=0.7	6.318	-0.1876	0.9792
R=0.8	6.597	-0.1668	0.9886

From Figure 4.3 can be seen that plotting the number of cycles against the stress amplitude converges to a single trend, with only a small variation for the different stress ratios. When looking at the spread of cycles to failure at a single amplitude, it can be seen that there is a small decrease in fatigue life for higher stress ratios, representing a larger mean stress. This difference is more apparent for the amplitudes below $0.1\sigma_y$.

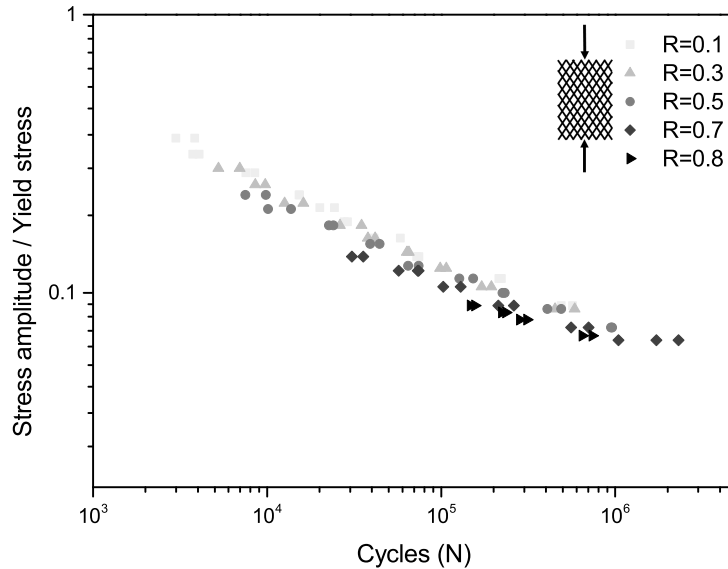
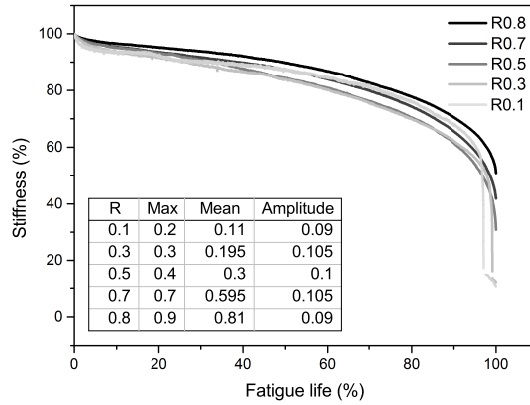


Figure 4.3: Normalized stress amplitude vs number of cycles to failure

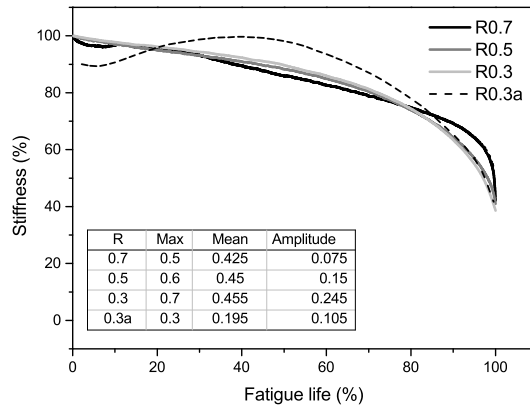
One way of presenting the gradual failure during the fatigue life of this type of samples, is plotting the total fatigue life against the stiffness of the specimens. This stiffness was calculated by dividing the maximum force with the corresponding displacement. This is not the actual stiffness, because the displacement at the minimum force also increases over the fatigue life. It can nevertheless be used to observe the gradual failure of the samples. The calculated stiffness values were normalized by dividing all values with the maximum stiffness to be able to compare different load cases. This was done in Figure 4.4 for tests with the same amplitude at different stress ratios. From this figure can be seen that all stress ratios showed a comparable decay. The final failure occurred at a lower stiffness decrease for maximum stresses above 0.4 or mean stresses higher than 0.3. This can be seen from the different end points of each line in the graph. The tests at $R=0.1$ and $R=0.3$ show a behavior which also occurred at a few other tests at low maximum stresses. The sample failed but could still take up loads before it reached the maximum displacement to trigger the test machine to stop. This can be observed by the short continuation of the line, after the large stiffness decrease. The number of cycles to failure of the experiments displayed in Figure 4.4a varied between approximately 130.000 and 225.000 for $R=0.3$ to $R=0.8$, and was around 560.000 cycles for $R=0.1$. An overview of the different normalized loads for each test is displayed in the table in the graph.

Because variations of the mean stress with constant amplitudes did not show significant differences, a second comparison is made in Figure 4.4b, of three different amplitudes at a mean stress around $0.45\sigma_y$. From this figure can be seen that the test at the lowest amplitude ($R=0.7$) has a constant decay comparable to the other tests, but over a longer period of the total fatigue life and a more rapid decrease near the end. The repeated tests that were performed under the same stress conditions showed the same behavior. The tests with an amplitude of $0.15\sigma_y$ and $0.245\sigma_y$ showed a very similar decay.

The test that is marked with $R=0.3a$ in Figure 4.4b, shows a stiffness increase during the test, which dropped again after around 50% of the fatigue life. This behavior occurred at four other tests, at different loading conditions. The total number of cycles did not deviate much from the repeated tests at the same conditions.



(a)



(b)

Figure 4.4: Stiffness decay over lifetime at a constant stress amplitude (a) and at increasing amplitudes (b)

4.4 Digital image correlation

From the DIC results (figure 4.5 - 4.7) can be seen that the feature detection algorithm does not always find corresponding points, especially for larger deformations. In Figures 4.5 and 4.6, the strain distribution halfway the fatigue life, and a few hundred cycles before failure is visualized, together with a plot of the strain data from the test machine. Figure 4.7 also shows the strain distribution at 75% of the total fatigue life. Three comparisons were made. In Figure 4.5, the strain distributions from two tests at $R=0.1$ have been observed. At 50% of the fatigue life, the strain distributions already indicate increased

strains at an angled orientation, which is more pronounced at the test with a lower maximum stress (B). The white line marks the direction of the final failure of the samples.

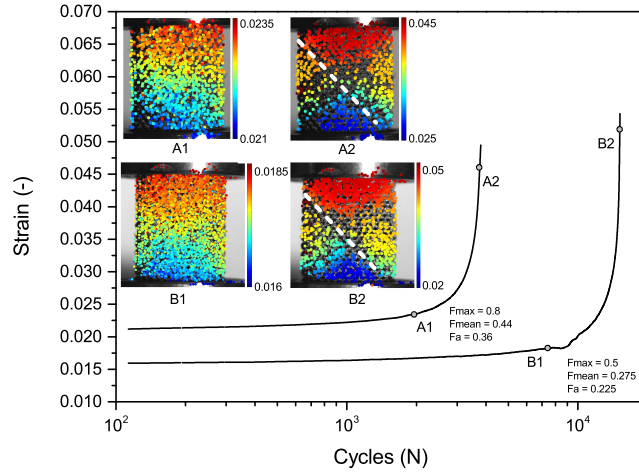


Figure 4.5: Strain development during Fatigue tests at $R=0.1$

The strain distribution at $R=0.5$ (Figure 4.6) shows more horizontal phases for the high maximum stress and amplitude(A1), while a clear difference is visible between the right upper half and left lower half of the specimen that is tested at lower loads(B1). This strain distribution suggests that the final failure would occur from the upper left to lower right, but as indicated by the white line it failed in the other direction.

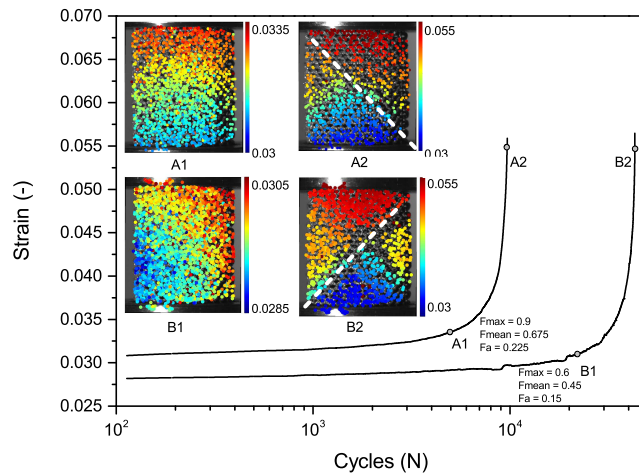


Figure 4.6: Strain development during Fatigue tests at $R=0.5$

In Figure 4.7, three different stress ratios with approximately the same amplitudes were compared. Specimen A was tested at an amplitude of $0.225\sigma_y$ with a maximum load of $0.9\sigma_y$, B at an amplitude of $0.28\sigma_y$ and maximum of

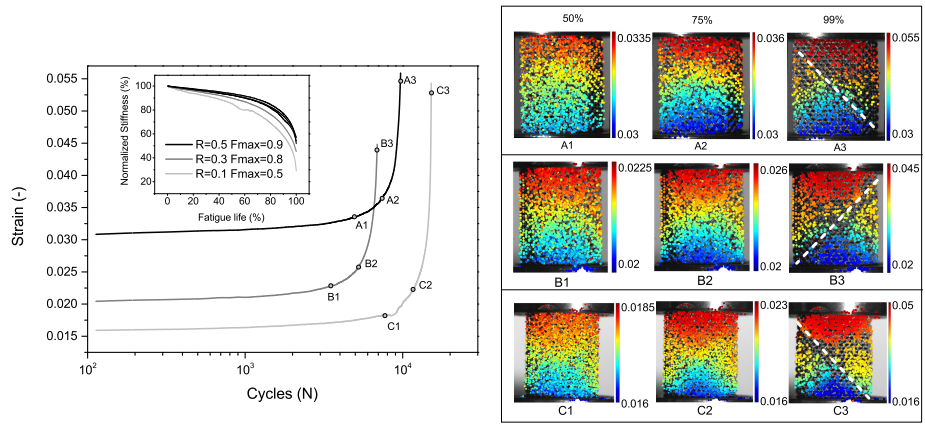


Figure 4.7: Strain development during Fatigue tests at equal amplitudes and different mean stresses($0.675\sigma_y$ (A), $0.52\sigma_y$ (B), $0.275\sigma_y$ (C))

$0.8\sigma_y$, and C at an amplitude of $0.225\sigma_y$ with a maximum load of $0.5\sigma_y$. For specimens B and C, a cross shape could already be observed halfway the fatigue life. From the inset graph can be seen that all tests showed a similar stiffness decay over the fatigue life, except for the test at $R=0.1$, which showed a faster stiffness decrease over the fatigue life. Two tests per load condition, one with DIC and one without are plotted in this graph. The strain values obtained from the DIC measurements correspond relative good to the strain values from the testing machine.

Chapter 5

Discussion

The results of the dry weighing and micro-CT measurements for the low porous sample showed a significant difference. This could be a result of possible entrapped powder that creates a larger weight than the actual solid struts. This powder could also be seen in the micro-CT images, where it proved to be difficult to separate this powder from the solid material during the image segmentation process.

Compression-compression fatigue tests would normally not cause fatigue failure, but different studies [30] [31] [29] have shown that porous structures fail due to compressive cyclic loading. The fatigue tests from this study confirmed the findings on porous materials, that the SN-behavior of compressive cyclic loading at stresses below the yield strength results in the same log-linear trend that is characteristic for tension-tension behavior. This study adds the effect of different stress ratios, which at first sight only leads to a shift of the SN-curves upwards with increasing stress ratio. This can be a result of lower stress amplitudes at increasing R-values, because the tests are based on predefined maximum loads.

No fatigue limit was observed during testing. All tests were continued until failure, with a maximum of $2 \cdot 10^6$ cycles for the lowest stress amplitude that was tested. Two fatigue tests were performed on the low porosity sample, at 0.6 and $0.7 \sigma_y$ with a stress ratio of 0.1. The test at $0.7 \sigma_y$ resulted in failure after $6 \cdot 10^5$ cycles, and the test at $0.6 \sigma_y$ was stopped after reaching well over a million cycles, without any signs of deterioration. The tests with the high porous samples showed that the fatigue life at these stress values would result in the lowest number of cycles compared to the whole test range. Therefore it was chosen not to do more tests with the low porosity samples.

The SN-curve comparison with a previous study from Amin Yavari et al. [29] in Figure 4.2, showed a close resemblance with the R=0.3 test. The reason that it does not fit with the R=0.1 results from this study, could be due to the smaller sample size that is used for those tests (10x15mm instead of 15x20mm). This can be an indication of a size effect which is known to occur for both smooth and notched specimens[52][11]. Tests with different sample sizes should be performed to prove if a size effect exists for these type of meta-biomaterials.

The decrease of the slope for higher R-ratios that is observed in Figure 4.2b by plotting the maximum stress and cycles on a logarithmic scale, indicates that only a small change of the maximum stress has a larger influence on the fatigue

life for higher stress ratios compared to lower stress ratios.

As already mentioned in the results section, a clear amplitude dependence on the fatigue life is observed when looking at Figure 4.3. The small effect of mean stress on the fatigue life can also be observed from a constant life diagram. In a constant life diagram, the combination of stress amplitude and mean stress is displayed for a specific number of cycles that will lead to failure. This was done with the test data in Figure 5.1, and for typical behavior of bulk Ti-6Al-4V in Figure 5.2. The values of the graph in Figure 5.1 are obtained from the exponential fit formulas. There is a small decrease of the stress amplitude visible when the mean stress is increased for fatigue lives of 50.000 and 100.000 cycles. The amplitude at 500.000 cycles does not seem to decrease at elevated mean stresses, it even shows a small increase of the allowable amplitude at a larger mean stress. The point that is indicated by the open box connected to a dotted line, is extrapolated outside the tested range. In most constant life diagrams, the theoretical intersection of the x-axis occurs at the ultimate stress of the material (in this case $1.3\sigma_y$), but no clear decline to this maximum could be observed.

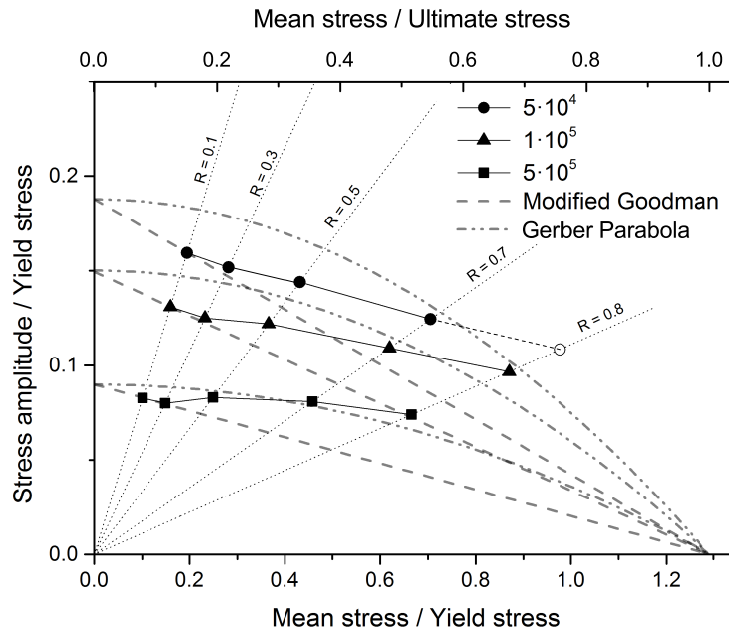


Figure 5.1: Constant life diagram constructed from test results

A common way of comparing or fitting data in constant life diagrams is by plotting the modified Goodman relation (equation 5.1). The test results are compared with this formula because it shows good correlation with different materials including Ti-6Al-4V. This formula predicts a linear decline between the fatigue life at fully reversed loading ($R = -1, \sigma_{mean} = 0$) to the ultimate stress of the material, where the amplitude is zero. Because the sample type that is used in this research cannot be tested in tension, the Goodman equation is rewritten to equation 5.2, which includes the $R = 0.1$ points (σ_{aR} and σ_{mR}) to be able to visualize this formula in relation to the test results. Other points

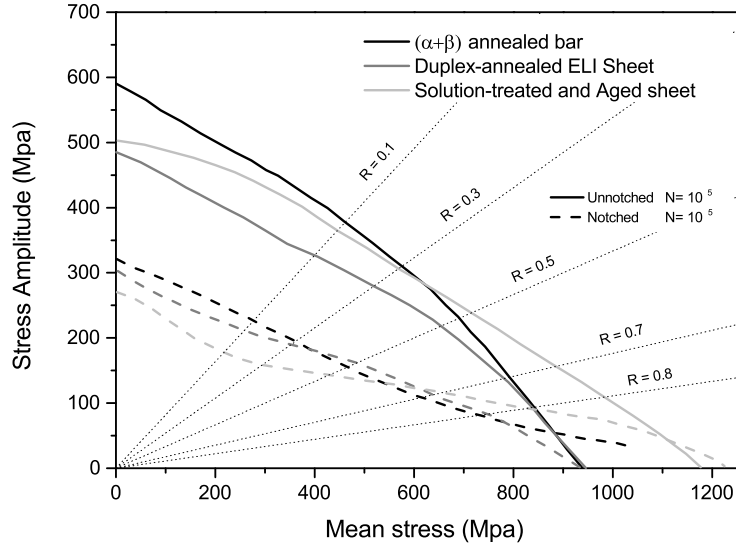


Figure 5.2: Constant life diagram comparing different Ti-6Al-4V compositions from [17]

to construct the modified Goodman relation could also have been chosen, but the $R = 0.1$ is selected because it is closest to the $R = -1$ value. Another common comparison that is used in fatigue diagrams is the Gerber parabola, which has the same axis intersections as the Modified Goodman relation but predicts a parabolic relation. Therefore the same axis intersections resulting from equation 5.2 are chosen for the Gerber parabola. The Goodman relation shows a correlation with the test data, only for the stress ratios $R=0.1$ and $R=0.3$. The Gerber parabola does only seem to fit the results at 500.000 cycles, for stress ratios of $R=0.5$, $R=0.7$ and $R=0.8$. Nevertheless, when looking at all data points for 500.000 cycles, no mean stress dependence is visible. It can therefore not be concluded that the R-ratio behavior follows the prediction of Goodman or Gerber.

$$\sigma_a = \sigma_{-1} \left(1 - \frac{\sigma_m}{\sigma_u} \right) \quad (5.1)$$

$$\sigma_a = \frac{\sigma_{aR} \sigma_u}{\sigma_u - \sigma_{mR}} \left(1 - \frac{\sigma_m}{\sigma_u} \right) \quad (5.2)$$

Fatigue diagrams of Ti-6Al-4V from literature all show comparable behavior, with a clear decline of the stress amplitude when the mean stress is increased. In order to compare these graphs from the literature with the test results of this study, three curves from the ASM international Fatigue data book (Henry et al. [17]) are digitized using a plot digitizer tool [53]. The data is plotted in Figure 5.2. The lines represent 10^5 cycles of both notched and smooth specimens for three different compositions. A significant R-ratio effect is observed for this material, which shows a similar behavior as predicted by the Gerber or modified Goodman relation. It can also be seen that the effect of notches results in a decrease of both the fatigue strength and mean stress sensitivity on the fatigue

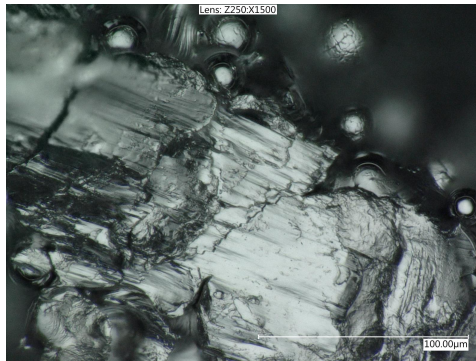
life. The study of Lanning et al. [24] also found similar behavior for notched specimens in comparison to smooth bar samples.

A method to quantify the notch effect is discussed by Nicholas [14] and Bell and Benham [54], where the (unnotched) data of the amplitude in a constant life diagram is reduced by a stress concentration factor k_t , or a fatigue notch factor k_f . Large values of these factors significantly reduce the slope of the curve and thereby lowering the mean stress dependence, which results in a curve on a constant life diagram that is similar to the notched behavior seen in Figure 5.2, which is comparable to the observations from the test results at 50.000 and 100.000 cycles (Figure 5.1).

The statement that notches could be the cause of the low mean stress sensitivity is also confirmed when looking at the surface of the sample (Figure 5.3a). Powder from the SLM process is visible on the surface and the overall appearance is very irregular. Observations from the fracture surface (Figure 5.3b) show multiple fatigue cracks that are initiated from a notch. Also the low scatter of the fatigue tests indicate that crack growth is dominant, which is usually a result of notches.



(a)



(b)

Figure 5.3: Close-up of strut at 250x magnification (a) Fracture surface with crack initiated from notch at a magnification of 1500x (b)

Previous fatigue tests on porous biomaterials used a 90% stiffness decrease as failure criterion. For this study, the failure criterion was set at 2mm displacement. All samples showed a steep decline of the stiffness at the end of the

fatigue life, resulting in a large increase of the displacement, triggering the test machine to stop.

From Figure 4.4 can be seen that not all test showed a decrease of stiffness as much as 90%. The reason that the minimum stiffness values at $R=0.5$ to $R=0.8$ did not reach values below 40% of the initial stiffness is a result of both the data sampling and failure criterion. The data sampling was set at an interval of 100 cycles, resulting in missing data on the final cycles before failure, where a large stiffness decrease occurs due to the increased displacements that eventually led to failure. The second reason is the failure criterion which was set at 2mm based on visual observations of the sample. The stiffness decrease for some samples only reached 40%, but were clearly failed based on their appearance.

As was mentioned in the results section, some tests showed an increase in stiffness without a significant difference in the fatigue life compared to the repeated tests (Figure 4.4b). A possible cause of this behavior could be a measurement error or a variation in the sample quality, but this could not be confirmed.

During all fatigue tests, failure occurred at a direction of 45 degrees. Most samples failed along one direction, while a few samples failed at both +45 and -45 degrees, resulting in a triangular or cross shaped failure (Figure 5.4). No relation was found between the applied loads and this failure appearance. The 45 degree failure direction was also observed during static compression tests of different porous structures by [39], [38], [55] and [37]. During the static compression tests, failure also occurred at 45 degrees, but more concentrated around the upper or lower area of the sample. At the same time, the struts that were in contact with the compression plate failed, after which the sample gradually crushed from this location.

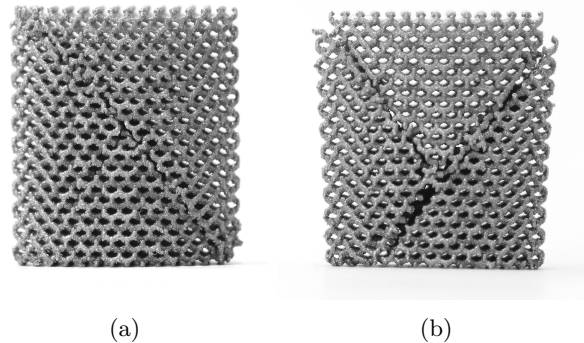


Figure 5.4: Typical fatigue failure at one (a) or two directions (b)

The displacement fields obtained by digital image correlation show that it is possible to visualize the failure direction and gradual deformation of the samples using relative simple methods, that have a good resemblance with the final failure direction. Comparisons between the DIC results for different load cases showed only small differences. At high maximum stresses the strain distribution is more horizontal, but this does not affect the final failure direction. Also no apparent differences were visible between the tests at the same stress ratios, except for one test that is displayed in Figure 4.6, where a clear upper and lower triangular part was visible in the strain distribution which did not correspond

with the final failure direction. Further investigation of the pictures from this test showed that the strain distribution changed gradually to the direction of final failure (Appendix B). More DIC tests can show if this behavior would occur more, but since the failure direction and total number of cycles did not deviate from the other tests, it is not investigated further. A possible reason for this behavior is a wrong sample alignment, which could be a result of non-parallel upper and lower faces of the sample.

The DIC results did also not show significant differences between the different R-ratio tests. For future research it can nevertheless be used to for example compare the behavior of different unit cell types. The image correlation results could also be further optimized by comparing different lightning conditions or adding non-reflective paint onto the specimens, because it was found that the samples were very reflective in the presence of a large light source that is needed in combination with the cameras. The increasing deformations of the sample during the test resulted in a change of the reflections which is unfavorable for the feature detection process.

As an extra comparison, images taken during two static compression tests are processed using the DIC Matlab script. These images are displayed in Figure C.2 and C.3, provided in Appendix C. In both figures, the total strain distribution is displayed next to the horizontal distribution. Both tests show a horizontal strain gradient that runs from top to bottom. The horizontal displacements show a different behavior, where in Figure C.3 a 45 degree separation is observed. This could be a result of nonparallel sample faces, which lead to a shear distortion. In Figure C.2 a vertical separation is observed, indicating a more homogeneous widening of the sample under its compressive load. Pictures were taken only during these two compression tests, which were shot manually every few seconds during the test. It is therefore not possible to compare the calculated strains with the test data from the machine. The results of the tests showed very little spread, indicating that the observed difference in strains of the two samples did not influence the results. It does however show that care must be taken to align the samples properly.

Chapter 6

Conclusions and Recommendations

6.1 Conclusions

The influence of R-ratio on the compression-compression fatigue behavior of porous titanium biomaterials made from a diamond unit cell was studied. The effect of stress ratio was investigated by constructing a constant life diagram and comparing the gradual failure under different loading conditions. An experimental DIC method was developed to aid in visualising the load distribution and damage mechanisms by motoring changes in the displacement field. Regarding the trends in the SN-behavior and constant life-diagrams of the porous biomaterial under investigation, the following concluding observations can be made:

- Compression-compression SN-behavior exhibits the same log-linear trend characteristic of the tension-tension behavior of the bulk material. This has also been confirmed by previous studies in the literature [30] [31] [29].
- The presence of a fatigue limit in the SN-behavior was not observed.
- An effect of R-ratio on the SN-behavior was observed, but is less pronounced for amplitudes below $0.1\sigma_y$ that result in a fatigue life of 500.000 cycles. Poor correlation between this observed R-ratio effect and the known R-ratio behavior of bulk titanium was found when comparing constant life diagrams.
- The R-ratio effect in the porous biomaterial showed a strong correlation with the stress amplitude, converging to a single trend line in the S-N graph.

Based on these observations and further investigation into the failure mechanisms, the following conclusions can be made:

- Low mean stress sensitivity in SLM manufactured biomaterials is similar to notched fatigue behavior of bulk Ti-6Al-4V. This could be a result of the high surface roughness that is caused by the SLM process.
- A gradual stiffness decrease was observed with similar rates of decay for different combinations of amplitude and mean stress.

- Fatigue failure at 45 degrees which is also observed in previous studies ([39], [38], [55], [37]), is independent of the applied loads and R-ratios.
- DIC can be used to visualize the 2D displacement field, showing locations with increased displacements that give an indication of the final failure shape.

6.2 Recommendations

The performed tests and results from this research have led to different questions that require further investigation beyond the scope of this project. These questions could provide subjects for new studies, or are aimed at improvement of the test results from this study, which is mainly focused on the DIC process. The recommendations are therefore divided in possible steps to follow up this research and recommendations to improve the DIC process.

The first recommendation is to test different porosity values. For this study, two 'extreme' porosity values were chosen to see if the porosity of the samples has an influence on the stress ratio behavior. The low porosity samples had such small pores that the specimen appeared to be solid. This resulted in a very large compressive stress, that damaged the compression plates of the test equipment. Two fatigue tests with this type of sample was performed, which resulted in failure after more than $6 \cdot 10^5$ cycles for 70% of the yield strength as maximum load. The test at the same normalized load of the high porous sample resulted in only 4000 cycles to failure. A sample with a larger porosity would be more suitable to test and should give insight in the effect of porosity on the stress ratio behavior. A second recommendation is to compare different unit cell types. Previous studies already showed that the fatigue behavior is depending on the unit cell type at a stress ratio of 0.1. This raises the question if different unit cell designs react different to the increased mean stress that is present at larger stress ratios. After comparing the test results of this research with previous studies, it was found that the SN behavior at $R=0.3$ was similar to the $R=0.1$ behavior of a previous study with the same test conditions, except for a different sample size. This could be an indication of a size effect, which can be verified by testing different sample sizes that have the same porosity value.

A last recommendation for extra tests is based on the hypothesis of this study that notches or surface roughness are the cause of the amplitude dependence on the fatigue behavior. Extra tests with for example heat treated specimens, or with a polishing finish could be conducted to verify this.

The second category of recommendations is focused on the DIC process. First it would be interesting to see if different unit cell designs show other local strains than the diamond unit cell structure. The DIC results from this study showed that it is possible to visualize the displacement field in these type of meta-biomaterials, which could for example be used to indicate weak points in the structure. These locations or specific struts could then be locally reinforced to improve the fatigue properties. But the DIC process that is developed for this project is far from perfect and can be improved in different ways. The first point that can be improved is the actual image capturing process. In standard DIC applications, usually flat specimens, a sample is painted white and a speckle pattern is applied to remove reflections and to create a random surface. The rough surface of the specimens resulted in a random surface, but

it was difficult to properly capture the samples without over- or underexposing the image. painting the sample would remove reflections but this also results in an even surface where distinctive features cannot be detected. Applying a speckle pattern proved to be very difficult, because of the small struts that the sample is made of. If this process is optimized, it could lead to a better and more accurate point detection of the software.

Another possible improvement that can be made for the image correlation process is the Matlab code. The code is for example not verified for accuracy and there are possible other methods to compare similar features in two images with Matlab. A different option is to try commercially available image correlation software, but this software is not always available and is optimized for the specific application of 'solid' specimens.

The last option to improve the digital image correlation method is to use two cameras instead of one. This makes it possible to create a 3D image that gives a better view of the displacement field, but the shallow depth of field of the cameras resulted in a blurred image. The depth of field could be increased by making the aperture of smaller, but this requires more light (which is easily provided with a lamp) which results in reflections and small overexposed points. Therefore the overall lighting method of the samples should first be improved before two cameras are applied.

Bibliography

- [1] Steve Amato and R Ezzell. *Regulatory Affairs for Biomaterials and Medical Devices*. Elsevier, 2014.
- [2] Michael N Helmus, Donald F Gibbons, and David Cebon. Biocompatibility: meeting a key functional requirement of next-generation medical devices. *Toxicologic pathology*, 36(1):70–80, 2008.
- [3] Marc Long and HJ Rack. Titanium alloys in total joint replacement a materials science perspective. *Biomaterials*, 19(18):1621–1639, 1998.
- [4] Coringroup. Hip implant, August 2015. URL http://www.coringroup.com/corin_corporate/image_library/.
- [5] Layerwise. Orthopedic implants with integrated bone scaffolds, July 2015. URL <http://www.layerwise.com/medical/markets/orthopedic/>.
- [6] Buddy D Ratner, Allan S Hoffman, Frederick J Schoen, and Jack E Lemons. *Biomaterials science: an introduction to materials in medicine*. Academic press, 2013.
- [7] Additively. Slm figure, September 2015. URL <https://www.additively.com/en/learn-about/laser-melting>.
- [8] Lore Thijs, Frederik Verhaeghe, Tom Craeghs, Jan Van Humbeeck, and Jean-Pierre Kruth. A study of the microstructural evolution during selective laser melting of ti-6al-4v. *Acta Materialia*, 58(9):3303–3312, 2010.
- [9] Seyed Mohammad Ahmadi, Saber Amin Yavari, Ruebn Wauthle, Behdad Pouran, Jan Schrooten, Harrie Weinans, and Amir A Zadpoor. Additively manufactured open-cell porous biomaterials made from six different space-filling unit cells: The mechanical and morphological properties. *Materials*, 8(4):1871–1896, 2015.
- [10] M. Janssen, J. Zuidema, and R. Wanhill. *Fracture Mechanics, Second Edition: Fundamentals and Applications*. Taylor & Francis, 2004. ISBN 9780203596869. URL <https://books.google.nl/books?id=yR06svyAko0C>.
- [11] Jaap Schijve. *Fatigue of Structures and Materials*. Springer, 2009. ISBN 978-1-4020-6807-2.

- [12] Norman E Dowling. *Mechanical behavior of materials: engineering methods for deformation fracture and fatigue*. Norman E. Dowling.: Pearson Prentice Hall, 2007. 912 p.; 26 cm. Pearson Prentice Hall, 2007.
- [13] Ralph I Stephens, Ali Fatemi, Robert R Stephens, and Henry O Fuchs. *Metal fatigue in engineering*. John Wiley & Sons, 2000.
- [14] Theodore Nicholas. *High Cycle Fatigue, a mechanics of materials perspective*. Elsevier Science Ltd, Oxford, 2006. ISBN 978-0-08-044691-2.
- [15] C. Leyens and M. Peters. *Titanium and Titanium Alloys: Fundamentals and Applications*. Wiley, 2006. ISBN 9783527605200. URL <http://books.google.nl/books?id=okSA1N1xAxgC>.
- [16] KJ Miller. Metal fatigue past, current and future. *Proceedings of the Institution of Mechanical Engineers, Part C: Journal of Mechanical Engineering Science*, 205(5):291–304, 1991.
- [17] S.D. Henry, K.S. Dragolich, N.D. DiMatteo, and ASM International. *Fatigue Data Book: Light Structural Alloys*. ASM International, 1994. ISBN 9781615031658.
- [18] JC Chesnutt, AW Thompson, and JC Williams. Influence of metallurgical factors on the fatigue crack growth rate in alpha-beta titanium alloys. Technical report, DTIC Document, 1978.
- [19] MJ Caton, R John, WJ Porter, and ME Burba. Stress ratio effects on small fatigue crack growth in ti-6al-4v. *International Journal of Fatigue*, 38:36–45, 2012.
- [20] J Ding, R Hall, and J Byrne. Effects of stress ratio and temperature on fatigue crack growth in a ti-6al-4v alloy. *International journal of fatigue*, 27(10):1551–1558, 2005.
- [21] J Lindemann and L Wagner. Mean stress sensitivity in fatigue of α , $(\alpha\beta)$ and β titanium alloys. *Materials Science and Engineering: A*, 234:1118–1121, 1997.
- [22] RJ Morrissey, DL McDowell, and T Nicholas. Frequency and stress ratio effects in high cycle fatigue of ti-6al-4v. *International Journal of Fatigue*, 21(7):679–685, 1999.
- [23] RJ Morrissey, DL McDowell, and T Nicholas. Strain accumulation in ti-6al-4v during fatigue at high mean stress. *Mechanics of Time-Dependent Materials*, 2(3):195–210, 1998.
- [24] David B Lanning, Theodore Nicholas, and George K Haritos. On the use of critical distance theories for the prediction of the high cycle fatigue limit stress in notched ti-6al-4v. *International journal of fatigue*, 27(1):45–57, 2005.
- [25] Yoshinori Ono, Tetsumi Yuri, Toshio Ogata, Saburo Matsuoka, and Hideo Sunakawa. Effect of stress ratio on high-cycle fatigue properties of ti-6al-4v eli alloy forging at low temperature. In *AIP Conference Proceedings*, pages 23–26, 2014.

- [26] Brecht Van Hooreweder, David Moens, Rene Boonen, Jean-Pierre Kruth, and Paul Sas. Analysis of fracture toughness and crack propagation of ti6al4v produced by selective laser melting. *Advanced Engineering Materials*, 14(1-2):92–97, 2012.
- [27] S. Leuders, M. Thne, A. Riemer, T. Niendorf, T. Trster, H. A. Richard, and H. J. Maier. On the mechanical behaviour of titanium alloy tial6v4 manufactured by selective laser melting: Fatigue resistance and crack growth performance. *International Journal of Fatigue*, 48:300–307, 2013.
- [28] Victoria Cain, Lore Thijs, Jan Van Humbeeck, Brecht Van Hooreweder, and Rob Knutsen. Crack propagation and fracture toughness of ti6al4v alloy produced by selective laser melting. *Additive Manufacturing*, 2014.
- [29] S. Amin Yavari, R. Wauthle, J. van der Stok, A. C. Riemsdag, M. Janssen, M. Mulier, J. P. Kruth, J. Schrooten, H. Weinans, and A. A. Zadpoor. Fatigue behavior of porous biomaterials manufactured using selective laser melting. *Materials Science and Engineering*, 33(8):4849–58, 2013.
- [30] S. Amin Yavari, S. M. Ahmadi, R. Wauthle, B. Pouran, J. Schrooten, H. Weinans, and A. A. Zadpoor. Relationship between unit cell type and porosity and the fatigue behavior of selective laser melted meta-biomaterials. *J Mech Behav Biomed Mater*, 43:91–100, 2015.
- [31] Nikolas W Hrabe, Peter Heintl, Brian Flinn, Carolin Körner, and Rajendra K Bordia. Compression-compression fatigue of selective electron beam melted cellular titanium (ti-6al-4v). *Journal of Biomedical Materials Research Part B: Applied Biomaterials*, 99(2):313–320, 2011.
- [32] G. Campoli, M. S. Borleffs, S. Amin Yavari, R. Wauthle, H. Weinans, and A. A. Zadpoor. Mechanical properties of open-cell metallic biomaterials manufactured using additive manufacturing. *Materials & Design*, 49:957–965, 2013.
- [33] S. M. Ahmadi, G. Campoli, S. Amin Yavari, B. Sajadi, R. Wauthle, J. Schrooten, H. Weinans, and A. A. Zadpoor. Mechanical behavior of regular open-cell porous biomaterials made of diamond lattice unit cells. *J Mech Behav Biomed Mater*, 34:106–15, 2014.
- [34] Ruben Wauthle, Bey Vrancken, Britt Beynaerts, Karl Jorissen, Jan Schrooten, Jean-Pierre Kruth, and Jan Van Humbeeck. Effects of build orientation and heat treatment on the microstructure and mechanical properties of selective laser melted ti6al4v lattice structures. *Additive Manufacturing*, 2014.
- [35] F Brenne, T Niendorf, and HJ Maier. Additively manufactured cellular structures: Impact of microstructure and local strains on the monotonic and cyclic behavior under uniaxial and bending load. *Journal of Materials Processing Technology*, 213(9):1558–1564, 2013.
- [36] B Gorny, T Niendorf, J Lackmann, M Thoene, T Troester, and HJ Maier. In situ characterization of the deformation and failure behavior of non-stochastic porous structures processed by selective laser melting. *Materials Science and Engineering: A*, 528(27):7962–7967, 2011.

- [37] SJ Li, LE Murr, XY Cheng, ZB Zhang, YL Hao, R Yang, F Medina, and RB Wicker. Compression fatigue behavior of ti-6al-4v mesh arrays fabricated by electron beam melting. *Acta Materialia*, 60(3):793–802, 2012.
- [38] XY Cheng, SJ Li, LE Murr, ZB Zhang, YL Hao, R Yang, F Medina, and RB Wicker. Compression deformation behavior of ti-6al-4v alloy with cellular structures fabricated by electron beam melting. *Journal of the mechanical behavior of biomedical materials*, 16:153–162, 2012.
- [39] O Cansizoglu, O Harrysson, D Cormier, H West, and T Mahale. Properties of ti-6al-4v non-stochastic lattice structures fabricated via electron beam melting. *Materials Science and Engineering: A*, 492(1):468–474, 2008.
- [40] Chunze Yan, Liang Hao, Ahmed Hussein, and David Raymont. Evaluations of cellular lattice structures manufactured using selective laser melting. *International Journal of Machine Tools and Manufacture*, 62:32–38, 2012.
- [41] R Hedayati, M Sadighi, M Mohammadi-Aghdam, and AA Zadpoor. Mechanics of additively manufactured porous biomaterials based on the rhombicuboctahedron unit cell. *Journal of the mechanical behavior of biomedical materials*, 53:272–294, 2016.
- [42] S. Amin Yavari, Ruben Wauthlé, Amarante J Böttger, Jan Schrooten, Harrie Weinans, and Amir Abbas Zadpoor. Crystal structure and nanotopographical features on the surface of heat-treated and anodized porous titanium biomaterials produced using selective laser melting. *Applied Surface Science*, 290:287–294, 2014.
- [43] J Kadkhodapour, H Montazerian, A Ch Darabi, AP Anaraki, SM Ahmadi, AA Zadpoor, and S Schmauder. Failure mechanisms of additively manufactured porous biomaterials: Effects of porosity and type of unit cell. *Journal of the mechanical behavior of biomedical materials*, 50:180–191, 2015.
- [44] A Zargarian, M Esfahanian, J Kadkhodapour, and S Ziaei-Rad. Numerical simulation of the fatigue behavior of additive manufactured titanium porous lattice structures. *Materials Science and Engineering: C*, 60:339–347, 2016.
- [45] Ruben Wauthle, Seyed Mohammad Ahmadi, Saber Amin Yavari, Michiel Mulier, Amir Abbas Zadpoor, Harrie Weinans, Jan Van Humbeeck, Jean-Pierre Kruth, and Jan Schrooten. Revival of pure titanium for dynamically loaded porous implants using additive manufacturing. *Materials Science and Engineering: C*, 54:94–100, 2015.
- [46] Ruben Wauthle, Johan Van der Stok, Saber Amin Yavari, Jan Van Humbeeck, Jean-Pierre Kruth, Amir Abbas Zadpoor, Harrie Weinans, Michiel Mulier, and Jan Schrooten. Additively manufactured porous tantalum implants. *Acta biomaterialia*, 14:217–225, 2015.
- [47] S. Amin Yavari, SM Ahmadi, Johan van der Stok, Ruben Wauthlé, AC Rienslag, M Janssen, Jan Schrooten, Harrie Weinans, and Amir Abbas Zadpoor. Effects of bio-functionalizing surface treatments on the mechanical behavior of open porous titanium biomaterials. *Journal of the mechanical behavior of biomedical materials*, 36:109–119, 2014.

- [48] ASTM B311. Standard test method for density of powder metallurgy (pm) materials containing less than two percent porosity. Technical report, ASTM International, 2013.
- [49] Michael Doube, Michał M Kłosowski, Ignacio Arganda-Carreras, Fabrice P Cordelières, Robert P Dougherty, Jonathan S Jackson, Benjamin Schmid, John R Hutchinson, and Sandra J Shefelbine. Bonej: Free and extensible bone image analysis in imagej. *Bone*, 47(6):1076–1079, 2010.
- [50] ISO. Iso 13314: Mechanical testing of metals - ductility testing - compression test for porous and cellular metals. Technical report, ISO, 2011.
- [51] Michael A Sutton, Jean Jose Orteu, and Hubert Schreier. *Image correlation for shape, motion and deformation measurements: basic concepts, theory and applications*. Springer Science & Business Media, 2009.
- [52] KH Kloos, A Buch, and D Zankov. Pure geometrical size effect in fatigue tests with constant stress amplitude and in programme tests. *Materialwissenschaft und Werkstofftechnik*, 12(2):40–50, 1981.
- [53] Ankit Rohatgi. Webplotdigitizer, October 2015. URL <http://arohatgi.info/WebPlotDigitizer>. Version 3.9.
- [54] WJ Bell and PP Benham. The effect of mean stress on fatigue strength of plain and notched stainless steel sheet in the range from 10 to 107 cycles. *ASTM STP*, 338:25–46, 1962.
- [55] Lijun Xiao, Weidong Song, Cheng Wang, Haiyan Liu, Huiping Tang, and Jianzhong Wang. Mechanical behavior of open-cell rhombic dodecahedron ti-6al-4v lattice structure. *Materials Science and Engineering: A*, 640: 375–384, 2015.

Appendix A

Matlab code DIC

```
clc
clear all
close all
%% Load and crop images

A=imread('Image_file');
B=imread('Image_file');

A1=imcrop(A, [544.5 454.5 1149 1152]);
B1=imcrop(B, [544.5 454.5 1149 1152]);

%% Determine number of pixels per mm, from three manual length measurements in image
P1=(979.08+986.57+986.57)/3;
mmpix=17.1/P1;

%% SURF points detection, with figure that displays the detected points
corners1 = detectSURFFeatures(A1,'MetricThreshold',1000);
corners2 = detectSURFFeatures(B1,'MetricThreshold',1000);
[features1, valid_corners1] = extractFeatures(A1, corners1);
[features2, valid_corners2] = extractFeatures(B1, corners2);
%%
indexCpairs = matchFeatures(features1, features2);
matchedcorners1 = valid_corners1(indexCpairs(:, 1));
matchedcorners2 = valid_corners2(indexCpairs(:, 2));
figure; ax=axes;
showMatchedFeatures(A1,B1,matchedcorners1, matchedcorners2);
%%
% plot(valid_corners);
legend(ax,'matched corners1', 'matched corners2');
title('SURFFeatures')
%calculate vector lengths
LengthsC1 = sqrt(((matchedcorners2.Location(:,1)-matchedcorners1.Location(:,1)).^2) +
((matchedcorners2.Location(:,2)-matchedcorners1.Location(:,2)).^2));

% Plot the vector lengths to see the spread
figure
plot(LengthsC1)
title('Before outlier filter')
xy=matchedcorners2.Location;
Lx=(matchedcorners2.Location(:,1)-matchedcorners1.Location(:,1));
Ly=(matchedcorners2.Location(:,2)-matchedcorners1.Location(:,2));
```

```

%% Remove outliers by calculation of the mean and standard deviation
mn = mean(LengthsC1);
st = std(LengthsC1);

[n,p] = size(LengthsC1);
% Create a matrix of mean values by
% replicating the mu vector for n rows
MeanMat = repmat(mn,n,1);
% Create a matrix of standard deviation values by
% replicating the sigma vector for n rows
SigmaMat = repmat(st,n,1);
% Create a matrix of zeros and ones, where ones indicate
% the location of outliers
outliers = abs(LengthsC1 - MeanMat) > 1.2*SigmaMat;
% Calculate the number of outliers in each column
nout = sum(outliers);
% Remove outlier points
LengthsC1(any(outliers,2),:) = [];
xy(any(outliers,2),:) = [];
Lx(any(outliers,2),:) = [];
Ly(any(outliers,2),:) = [];

%% calculate deformation in mm
LengthsC = ((LengthsC1*mmpix)+0.31)/19.4;
Lx=Lx*mmpix;
Ly=Ly*mmpix;
figure
plot(LengthsC1)
title('After removing outliers')

%% set x and y coordinates for scatter plot

X = double(xy(:,1));
Y = double(xy(:,2));
Z = double(LengthsC);

%% Colormap plot with displacements
figure
imshow(B1)
freezeColors % External Matlab Package to add colormap on top of scatter plot
hold on;
s1=scatter(X,Y,100,Z,'fill');
colormap(jet);
caxis([0.016 0.023])

colorbar
c = colorbar;
c.Label.String = 'Strain(-)';
axis off

```

Appendix B

Extra Images DIC

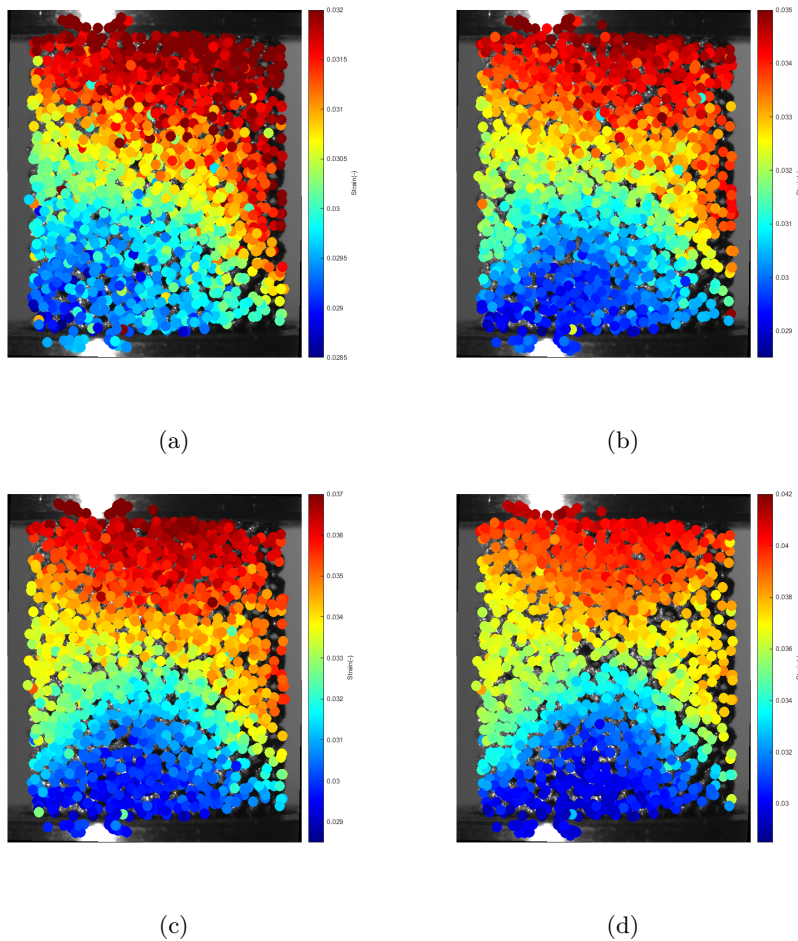


Figure B.1: Strain distribution during fatigue at 75% (a) 85% (b) 90% (c) and 95% (d) of the total fatigue life

Appendix C

Compression Test and DIC

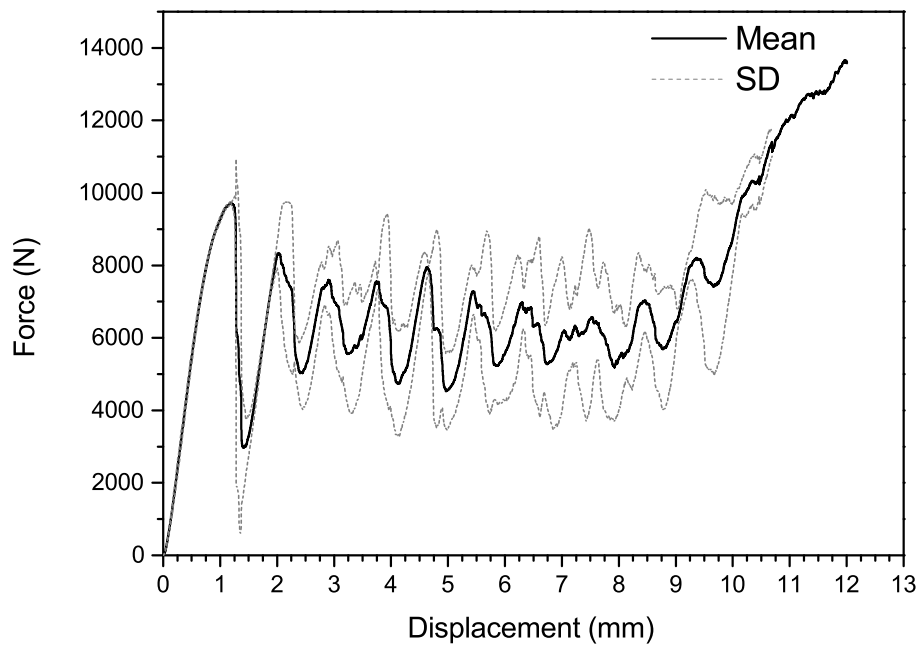


Figure C.1: Force displacement curve from 80% porous samples

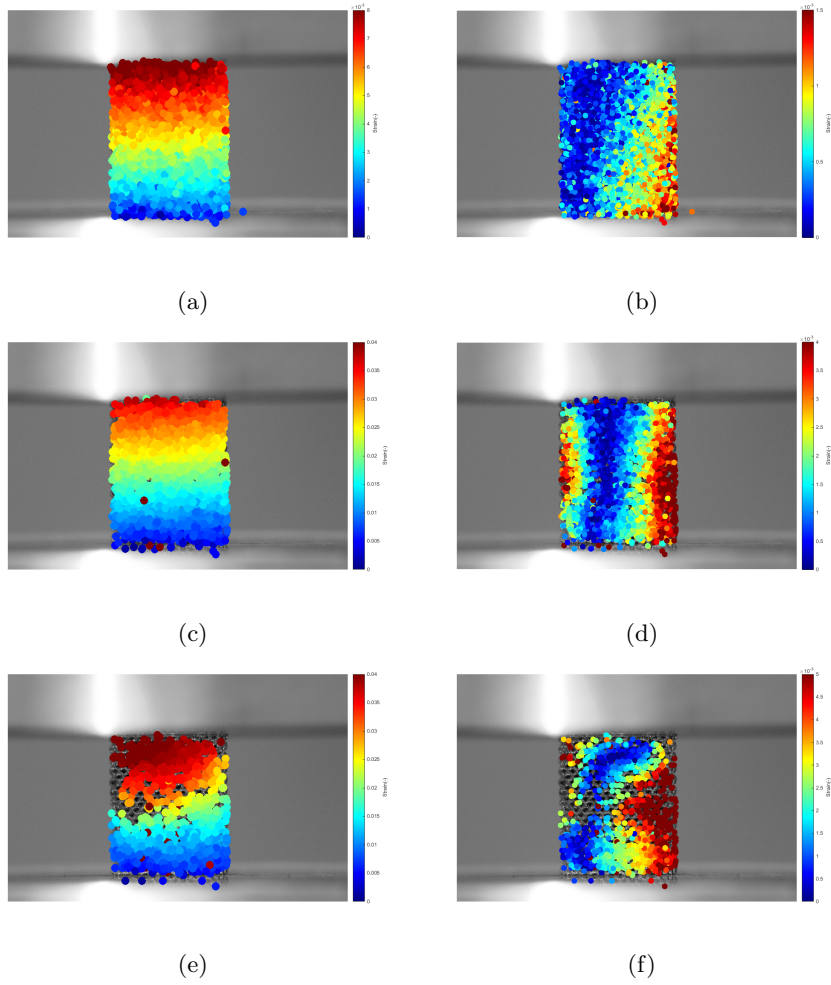


Figure C.2: Strain distribution during compression at start of test (a), halfway first failure (c) and after first failure (e) horizontal distribution at start (b), halfway (d) and after first failure (f)

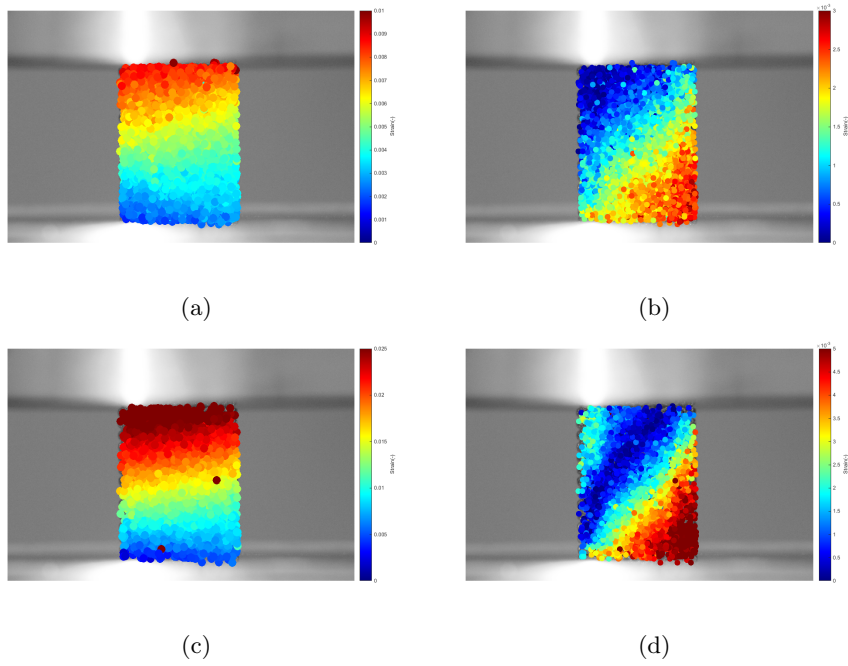


Figure C.3: Strain distribution during compression at start of test (a), just before first failure (c) horizontal distribution at start (b) and just before failure (d)

Appendix D

Sample overview

Table D.1: Sample overview part 1 of 3

Sample nr	Length	R	Fmax	Cycles to failure	Comments
S1-S5					Static tests
S6	19.45	0.1	0.5	19400	Wrong failure criteria (10mm) total 30758 cycles, 2mm failure cycles taken from data
S7	19.4	0.1	0.5	15352	+ pictures
S8	19.4	0.1	0.5	15238	+ pictures
S9	19.42	0.1	0.6	7546	-1mm displacement after test start
S10	19.42	0.1	0.6	8501	Same data file as S9
S11	19.4	0.1	0.7	4064	
S12	19.39	0.1	0.7	3737	
S13	19.46	0.1	0.45	24388	
S14	19.42	0.1	0.45	20047	
S15	19.4	0.1	0.4	28947	
S16	19.34	0.1	0.4	27725	
S17	19.4	0.1	0.35	41136	
S18	19.39	0.1	0.35	58233	
S19	19.36	0.1	0.3	74561	
S20	19.34	0.1	0.3	72278	
S21	19.42	0.3	0.7	8555	
S22	19.43	0.3	0.7	9737	
S23	19.41	0.3	0.6	16144	
S24	19.5	0.3	0.6	12608	
S25	19.51	0.3	0.45	38002	
S26	19.41	0.3	0.45	41728	
S27	19.51	0.3	0.4	63661	
S28	19.41	0.3	0.5	34919	+ pictures
S29	19.42	0.1	0.8	3828	+ pictures
S30	19.18	0.1	0.8	2988	+ pictures
S31	19.34	0.3	0.8	6969	+ pictures

Table D.2: Sample overview part 2 of 3

Sample nr	Length	R	Fmax	Cycles to failure	Comments
S32	19.29	0.3	0.8	5252	+ pictures
S33	19.42	0.3	0.4	65350	
S34	19.42	0.1	0.25	221842	
S35	19.3	0.3	0.25	451577	
S36	19.49	0.3	0.5	26200	
S37	19.42	0.5	0.8	13734	
S38	19.3	0.5	0.8	10133	
S39	19.42	0.5	0.7	24005	
S40	19.41	0.5	0.5	64411	
S41	19.38	0.5	0.5	74057	
S42	19.3	0.5	0.6	39134	
S43	19.38	0.5	0.6	44215	
S44	19.28	0.5	0.7	22639	
S45	19.3	0.5	0.25	-	Stopped after 831536 cycles (Expected to not fail)
S46	19.4	0.8	0.8	-	Stopped after 205260 cycles (test could not be continued due to machine reservation)
S47	19.41	0.3	0.35	106851	(separated in two parts)
S48	19.51	0.3	0.35	98463	
S49	19.43	0.5	0.45	152566	
S50	19.41	0.5	0.3	959318	
S51	19.49	0.5	0.45	126925	
S52	19.25	0.5	0.3	943440	
S53	19.35	0.5	0.4	224595	
S54	19.44	0.3	0.3	171040	
S55	19.23	0.3	0.3	194185	
S56	19.33	0.5	0.35	488933	
S57	19.29	0.5	0.4	231464	
S58	19.42	0.7	0.8	57059	
S59	19.38	0.7	0.8	74153	
S60	19.31	0.7	0.5	703634	
S61	19.32	0.7	0.7	129161	
S62	19.2	0.7	0.7	102597	
S63	19.37	0.7	0.8	73409	

Table D.3: Sample overview part 3 of 3

Sample nr	Length	R	Fmax	Cycles to failure	Comments
S64	19.46	0.7	0.5	557089	
S65	19.2	0.7	0.6	212670	
S66	19.31	0.7	0.6	261676	
S67	19.45	0.7	0.45	1044782	
S68	19.32	0.1	0.25	214588	
S69	19.34	0.7	0.45	2309803	
S70	19.34	0.7	0.9	35653	
S71	19.09	0.7	0.9	30707	
S72	19.44	0.5	0.9	9808	
S73	19.31	0.5	0.9	7481	
S74	19.3	0.3	0.25	585251	
S75	19.42	0.8	0.9	146935	
S76	19.33	0.8	0.9	156038	
S77	19.48	0.5	0.35	407580	
S78	19.29	0.8	0.85	235124	
S79	19.35	0.1	0.2	488497	
S80	19.37	0.8	0.85	222415	
S81	19.5	0.1	0.2	567840	
S82	19.45	0.8	0.8	310301	
S83	19.44	0.8	0.7	737501	
S84	19.52	0.8	0.8	281788	
S85	19.5	0.8	0.7	646537	
S86	19.45	0.7	0.45	1724591	
S87	19.38	0.5	0.9	9797	+ pictures
S88	19.48	0.5	0.6	43127	+ pictures
S89	19.55	0.5	0.9	8181	+ pictures
S90	19.61	0.1	0.7	653565	Low porosity sample
S91	19.65	0.1	0.6	1242060	Low porosity sample, no failure after +1million cycles

Appendix E

Paper abstract and introduction

abstract

Meta-biomaterials are porous biomaterials created by additive manufacturing techniques such as Selective Laser Melting. These materials are built up from a repeating unit cell, resulting in a porous structure that can be applied for bone implants or prosthetics. The mechanical properties of these meta-biomaterials can be tailored by variations in unit cell type and strut thickness, resulting in different porosity values. This makes it possible to create a material with mechanical properties similar to bone, which prevents negative side effects of conventional bone implants such as stress shielding. The fatigue behavior of these meta-biomaterials has been studied before, but only at a single stress ratio of $R=0.1$. This study investigates the fatigue behavior at different stress ratios which result in an increased mean stress. A cylindrical porous structure that is built up from a diamond unit cell is tested at stress ratios of $R=0.1$, $R=0.3$, $R=0.5$, $R=0.7$ and $R=0.8$. The sample is made of Ti-6Al-4V ELI powder, and has a theoretical porosity of 80 and 10%. Also an experimental DIC method is developed, to visualize the deformation behavior during the fatigue tests. A strong amplitude dependence on the fatigue life was found, with only little effect of the mean stress. This poorly correlates with the known R-ratio behavior of bulk titanium, that shows a clear decrease of the fatigue life with increasing mean stress. All tests showed a clear failure direction of 45 degrees, which could also be observed from the displacement field of the DIC results. The low mean stress sensitivity could be a result of the high surface roughness that is caused by the SLM process.

Introduction

Additive manufacturing techniques like Selective Laser Melting (SLM) and Electron Beam Melting (EBM) are increasingly used for biomaterials because of the design freedom, high precision and ability to produce parts directly from a CAD design without the need for molds (Thijs et al. [8]). This is especially useful

for bone implants, that consist of a porous structure, and which for example need to be patient specific. This has led to the development of a new material group called meta-biomaterials (Amin Yavari et al. [30]). This term describes additively manufactured porous materials that are built up from repeating unit cells from which they derive their mechanical properties. This expression is developed to distinguish these type of materials with other meta-materials, or biomaterials that are produced with conventional techniques.

Selective Laser Melting is a process that uses a laser to locally melt a thin layer of metal powder, which then solidifies in the desired cross-sectional shape. A new layer is placed on top of the previous, after which the process is repeated until the full part is built. The most common material that is currently used for this manufacturing process is Ti-6Al-4V.

Because of high temperature gradients during the SLM process, unfavorable microstructures and residual stresses develop in the material. Different studies focused on the mechanical properties of SLM produced parts. The studies of Van Hooreweder et al. [26], Cain et al. [28] and Leuders et al. [27] showed among others that the fracture toughness and crack growth rate of SLM produced parts are inferior to parts made with conventional techniques, but can be significantly improved with different heat treatments.

A lot of attention has also been given to the fabrication of cellular lattice structures, with designs that were impossible to produce using conventional methods. These structures are made either by EBM (Li et al. [37], Cansizoglu et al. [39], Cheng et al. [38], Hrabe et al. [31]) or with SLM (Yan et al. [40] Gorny et al. [36], Brenne et al. [35]).

The potential for manufacturing such lattice structures makes SLM processes attractive to the biomedical field. Bone implants require an open or porous structure to allow for bone ingrowth, and need to have mechanical properties comparable to bone to prevent stress shielding (Ratner et al. [6]). Also a fatigue life of at least one million cycles is required.

Meta-biomaterials are characterized by a specific unit cell and porosity or relative density value. A structure is created by repeating a single unit cell design in all directions. Examples of these unit cell types are Diamond, Cubic, Rhombicuboctahedron or Truncated Cuboctahedron, which result in different mechanical properties (Ahmadi et al. [9]). The porosity value is determined by the strut thickness of the unit cells and their size, which has an influence on the mechanical properties (Amin Yavari et al. [29], Amin Yavari et al. [30], Hedayati et al. [41]). Other research on this topic has aimed at the effect of build orientation and heat treatments (Wauthle et al. [34]), the development of the microstructure (Amin Yavari et al. [42]) and Finite Element simulations (Ahmadi et al. [33], Campoli et al. [32], Kadkhodapour et al. [43], Zargarian et al. [44]). All studies mentioned in this paragraph are based on Ti-6Al-4V, but development of the SLM process also made it possible to produce pure titanium (Wauthle et al. [45]) and Tantalum (Wauthle et al. [46]) meta-biomaterials.

Only few studies looked at the fatigue properties of meta-biomaterials, including Amin Yavari et al. [29], Amin Yavari et al. [30] and Hrabe et al. [31]. These studies investigated the effect of unit cell type and porosity on the fatigue life of meta-biomaterials. What not has been researched is the effect of different fatigue load cases.

A standard sinusoidal fatigue cycle can be described by its minimum, maximum and mean stress, where the ratio between min and max is defined as the

R-ratio. All previous tests are performed at an R-ratio of 0.1, meaning that the maximum stress is ten times the minimum stress. Increasing this stress ratio results in a higher mean stress, which is known to result in a much lower fatigue life for bulk Ti-6Al-4V (Nicholas [14], Henry et al. [17], Lindemann and Wagner [21]). The so called R-ratio behavior is normally a material specific characteristic, which raises the question if the behavior of meta-biomaterials follows the same trend as the material that it is made of. It is expected that if the behavior is different, a trend towards the bulk material behavior could be observed when decreasing the porosity value, resulting in a more solid sample. For this research, a very high and very low porosity sample is tested at different R-ratios to construct a constant life diagram, which can then be used to compare the R-ratio behavior. The R-ratio behavior can also be referred as the stress ratio behavior of mean stress behavior.